A SIMPLE TECHNIQUE TO IMPROVE THE LINEARITY AND FIELD-OF-VIEW OF CROSSED ANODE WIRE POSITION SENSITIVE PHOTOMULTIPLIER TUBES

by

Raymond Lecours Clancy

A thesis submitted to the Faculty of Graduate Studies and Research in partial fulfillment of the requirements for the degree of

Master of Engineering

McGill University

November, 1998

Department of Biomedical Engineering

0-612-50597-9

McGill University
Abstract

A Simple Technique to Improve the Linearity and Field-of-view of Crossed Anode Wire Position Sensitive Photomultiplier Tubes

by Raymond Lecours Clancy

Supervisor: Professor C. J. Thompson
Department of Medical Physics

Crossed anode wire position sensitive photomultiplier tubes (PS-PMTs) detect the location of a light source and provide the X and Y coordinates of the events. These coordinates are typically generated using Anger logic, where a resistor chain divides the current flow into two signals for each coordinate (X^+, X^- & Y^+, Y^-). In the standard readout, identical resistor values are used across the entire resistor chain. While this arrangement provides a linear readout in the central portion of the photomultiplier face, the readout is non-linear and sometimes even double valued near the edges of the PS-PMT due to the truncation of the charge beyond the last anode wire. To counter this effect, we have increased the value of the resistance near the ends of each resistor chain in order to compensate for the charge lost beyond the anode wires. Measurements were made using a Hamamatsu R-3941 PS-PMT coupled to a pixellated BGO matrix of cut crystals with a 2 mm pitch in each direction. After changing the end resistors, the usable field-of-view increased by 39%. This simple modification should enhance the operation of PS-PMTs in application such as positron emission mammography, and small animal PET imaging.

Université McGill

Résumé

Une méthode simple pour améliorer la linéarité et le champ de vue de tubes photomultiplicateurs sensibles à la position.

par Raymond Lecours Clancy

Superviseur: Professeur C. J. Thompson
Département de Physique Médical

Les tubes photomultiplicateurs (TPM) sensibles à la position sont capables de déterminer la position d'une source de lumière et de générer les coordonnées de l'évènement selon les axes X et Y. Ces coordonnées sont typiquement générées en utilisant la méthode Anger, où une chaîne de résistances divise les courants produits sur les anodes en deux signaux pour chacune des coordonnées (X^+, X^- et Y^+, Y^-). Des résistances identiques sont habituellement utilisées dans la chaîne. Bien que cette méthode fournisse une lecture de position linéaire dans la partie centrale du TPM, la mesure devient non-linéaire, et même non-univoque, à l'approche de la périphérie de la photocathode. Afin de corriger cet effet, nous proposons d'augmenter la valeur des résistances placées aux extrémités de la chaîne de résistance pour compenser la perte de charges au-delà des derniers fils de l'anode. Des essais ont été effectués avec un tube R-3941 de la compagnie Hamamatsu et une matrice de cristaux de BGO ayant une séparation de 2 mm dans chaque direction. En changeant les deux résistances aux extrémités de chaque axe du TPM, le champ de vue augmente de 39%. Cette simple modification pourrait améliorer la perfomance des TPM de position dans plusieurs applications comme, par exemple, en mammographie par émission de positron ou dans les systèmes de tomographie d'émission par positrons pour petits animaux.

TABLE OF CONTENTS

LIST OF FIGURES

ACKNOWLEDGMENTS

The author wishes to gratefully acknowledge grants from the National Cancer Institute of Canada's Breast Research Initiative (grant #6139) and the National Science and Engineering and Research Council of Canada (grant #36672) which helped support research and development of the Montreal Neurological Institute's positron emission mammography system.

I would like to thank the many individuals who have contributed to the work described in this thesis. Dr. C. J. Thompson, as my supervisor and mentor provided the necessary guidance and enthusiasm to ensure the successful completion of the PEM project. I want to thank my fellow students for the many rewarding hours spent learning and developing the MNI PEM system. Dr. T. Yamashita of Hamamatsu Photonics, who answered my many questions regarding crossed anode position sensitive photomultiplier tubes, also deserves my gratitude.

Finally, I want to thank my parents, Steve Clancy and Pauline Lecours Clancy and my fiancée, Alexandra Chiara. Without their constant encouragement and dedication, none of this would have been possible.

INTRODUCTION

Over 1600 Canadian women are diagnosed with breast cancer each year [1]. Consequently, research efforts to improve the effectiveness of diagnostic equipment used in the diagnoses and treatment of this disease have taken on special importance. One of the most exciting and promising current areas of research in this field is the development of a low-cost high-resolution functional imaging system: *positron emission mammography* (PEM) [2,3,4].

PEM systems use photomultiplier tubes coupled to scintillation crystals in order to convert gamma rays into an electrical signal. These gamma rays are the result of positron annihilation events occurring within the patient's body. PEM systems can differentiate between cancerous and benign sites in the breast because of the preferential uptake of an injected positron emitting radiopharmaceutical, such as *2-[^{18}F]-fluoro-2-deoxy-D-glucose* (FDG) by active cancerous cells [5,6]. This phenomenon allows PEM to capture a functional image of cellular metabolism.

Mammography, the standard breast cancer imaging system, produces very high-resolution structural images of the tissue density within the breast. Unfortunately, when this method is used to identify a possible tumor, it produces a high rate of false-positive diagnoses. Diagnoses are then followed by needle biopsies of the suspicious sites and subsequent analysis to determine whether sites are benign or cancerous.

In order to reduce the number of unnecessary needle biopsies, a PEM system developed at the *Montreal Neurological Institute* (MNI) is being used in conjunction with a standard mammography system. The mammogram provides structural information regarding the density of breast tissue, while PEM offers functional information about the metabolic uptake of an injected radiopharmaceutical. It is hoped that the combined information gathered from a mammogram and a PEM scan will significantly reduce the need for needle biopsy procedures while aiding in the assessment of chemotherapy outcome [7]. It may also significantly improve the information available to oncologists in their treatment planning. Therefore, PEM holds the potential to significantly improve the lives of Canadian women and their families.

Maximizing the field-of-view of the detectors of the MNI-PEM system is a crucial step in maximizing the system's ability to effectively identify cancerous breast tumors. In PEM, the dead space surrounding the *position sensitive photomultiplier tube* (PS-PMT) limits the ability of the PEM system to detect tumors located near the chest wall. The greater the dead space surrounding the detector the further away the useful imaging field is from the chest wall. As will be demonstrated in this thesis, modifications to the readout of PS-PMTs can significantly reduce this dead-space and thereby facilitate the detection of cancerous tumors located near the chest wall.

This thesis describes a technique that can be applied to PS-PMT anode wire resistive chains in order to increase the field-of-view and the linearity of the readout. Although this technique is simple, it is of critical importance in maximizing the MNI-PEM system's ability to identify cancerous tumors and reduce the number of unnecessary needle biopsies performed each year. In order to facilitate understanding this technique, the physical laws governing the behaviour of photomultiplier tubes and some readout methods currently used to determine the PS-PMT event positioning will be described.

Chapter 1

GAMMA RAY DETECTION

Gamma rays (γ-rays) are high-energy photons with wavelengths shorter than 10^{-11}m. They are difficult to observe because of their high energy. Detectors combining inorganic scintillation crystals and photomultiplier tubes were developed to make it possible to observe γ-rays. Much work has gone into the development of both scintillation crystals and photomultiplier tubes. These two are used together to capture γ-rays and convert them into useful information in various fields including medical imaging [8,9], astronomy [10], oil well logging [11] and nuclear radiation contamination detection [12,13]. In order to maximize the rate of interactions with γ-rays, scintillation materials must be very dense. They must also produce a signal that is accurate and easily adaptable for use with standard metnods of electronic data collection.

In this chapter, we will focus on γ-ray detection developments for medical imaging applications such as *positron emission tomography* (PET) and *single photon emission computed tomography* (SPECT). However, these developments equally apply to other fields.

1.1 Scintillation Crystals

Scintillation crystals play a crucial role in the detection of gamma ray energy. They are the first line of contact with the incoming high-energy photons. They must capture the incident photons and efficiently convert them into lower energy photons capable of being easily detected by a photodetector.

Scintillation crystals produce luminescence when they interact with sufficiently high energy photons. Scintillators convert energy deposited by ionizing radiation into lower energy photons as they interact within the material. Most commonly used scintillation crystals produce photons in the upper visible and ultraviolet spectra.

Effective scintillation crystal materials must possess a number of characteristics. They must have a high energy-conversion efficiency. They must have a short decay time constant and have a high density in order to stop photons in the shortest distance possible. They must convert the energy of the incoming gamma ray into photons of frequencies that correspond to those that the photodetector is most sensitive.

1.1.1 Photon Matter Interaction

As high-energy photons enter scintillation crystals they interact with the crystal material and often produce photons of lower energy. High energy gamma rays such as those found in PET and SPECT imaging typically have two principal modes of interacting with the scintillation crystal: photoelectric interactions and Compton scatter.

Photoelectric Effect

Albert Einstein won the Nobel Prize for his pioneering work on the photoelectric effect in 1921. He developed a formula (see equation(1)) relating the energy of a photon (E_γ=hν) striking a material, to the energy (E_e) of the resulting escaping electrons.

$$E_e = \tfrac{1}{2} m_e v^2 = E_\gamma - \phi = h\nu - \phi \tag{1}$$

The photon provides the energy necessary to overcome the binding energy or work function (ϕ) of the material and the rest of the imparted energy remains with the electrons. This causes the release of electrons from the atom. The loss of the electrons and creation of corresponding holes elevates the atom to an excited state. In order for the atom to return to its preferred ground state, an electron from a higher energy shell fills the hole. This causes the release of a number of photons with a combined energy $h\nu$, which corresponds to the difference of energy between the electron shells.

Compton Scattering

There is a finite probability for each material that the incident photons will interact with free electrons in the scintillation medium. As these interact, the photon imparts part of its momentum and energy to the electron. Figure 1 shows the result of such an interaction.

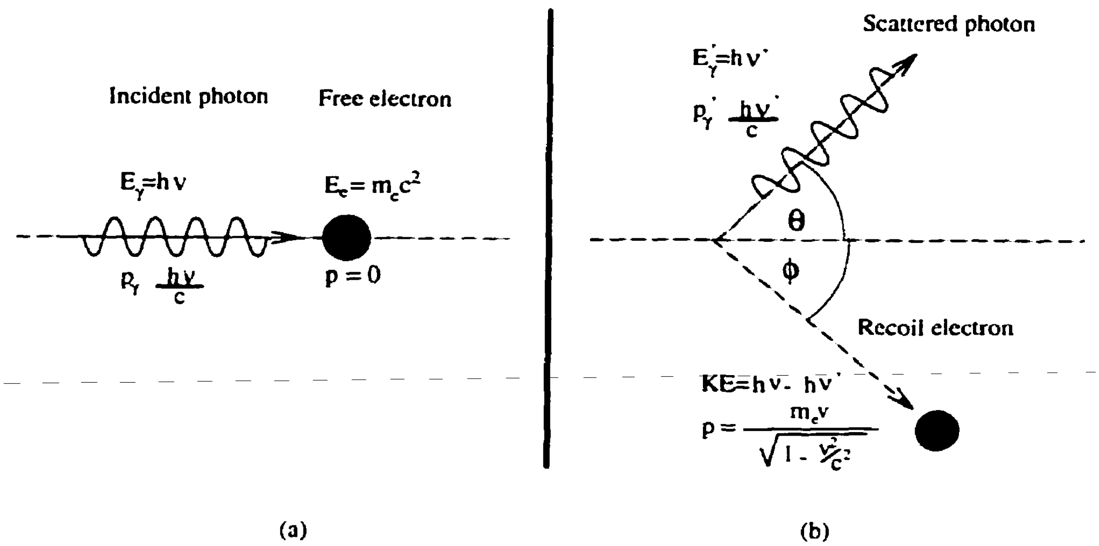

Figure 1 Compton scattering interaction.

A photon with energy, $E\gamma = h\nu$ interacting with a free electron will impart a fraction of its energy to the electron. As a result, the photon will have a lower frequency ν' and will impart kinetic energy, KE to the electron [14]. Equation(2) describes this kinetic energy.

$$KE = h\nu - h\nu' = m_e c^2 \left(\frac{1}{\sqrt{1 - \frac{v^2}{c^2}}} - 1 \right) \tag{2}$$

The interaction between the photon and the electron will also cause a deflection of both the photon and the electron. Knowing the initial photon energy, $E\gamma$ and the angle of deflection θ, the kinetic energy (KE) can also be described by equation(3)

$$KE = h\nu \cdot \frac{\alpha\,(1 - \cos\theta)}{1 + \alpha\,(1 - \cos\theta)} \tag{3}$$

where α is defined as,

$$\alpha \equiv \frac{h\nu}{m_e c^2} = \frac{h\nu}{511KeV} \tag{4}$$

Similarly, the energy of the resultant photon after a Compton scattering interaction with a deflection angle of θ is described by equation(5).

$$h\nu' = h\nu \cdot \frac{1}{1 + \alpha\,(1 - \cos\theta)} \tag{5}$$

Linear Attenuation

Different scintillators have different probabilities of interacting with photons. For a given incident photon flux, $\Phi(x)$ the absorption of flux by the scintillation crystal is proportional to the photon flux itself. The ability of particular materials to attenuate the energy of the incoming photons is determined by the proportionality constant which is also known as the linear attenuation coefficient, μ found in equation(6).

$$\frac{d\Phi(x)}{dx} = -\mu\,\Phi(x) \tag{6}$$

Solving the differential equation(6) produces a function relating the attenuated flux after reaching distance, x within a material with a linear attenuation coefficient μ (see equation(7)).

$$\Phi(x) = \Phi(0)\,e^{-\mu x} \tag{7}$$

The linear attenuation constant is proportional to the atomic number of the material as well as to its density. For gamma ray imaging purposes μ is related to the probability of a photoelectric interaction and the probability of Compton scattering.

1.1.2 Characteristics of Scintillation Crystals

Over the years, many scintillation crystals have been discovered with a wide range of properties. Table 1 contains a list of several commonly used scintillation crystals in the medical imaging field along with some of their characteristics.

Scintillator Composition	*Density (g/cm^3)*	*Index of refraction*	*Wavelength of maximum emission (nm)*	*Decay time constant (ns)*	*Scintillation pulse height*[1]
NaI	3.67	1.78	303	60	190
NaI(Tl)	3.67	1.85	410	230	100
CsI	4.51	1.80	310	10	6
CsI(Tl)	4.51	1.80	565	1000	45
BGO ($Bi_4Ge_3O_{12}$)	7.13	2.15	480	300	10
GSO	6.71	1.9	440	60	20
BaF_2	4.88	1.49	220/310	0.6/630	5/15
YAP	5.50	1.9	370	30	40
LSO	7.40	1.82	420	42/12	143

Table 1 Properties of some commonly used scintillator crystals.[15,16,17,18]

Scintillation pulse output size is one of the most important characteristics of a scintillation crystal. It determines the detection sensitivity that can be attained. Crystals such as NaI and NaI(Tl) produce very high numbers of photons per interaction. Unfortunately, these materials are hygroscopic which makes them difficult to handle. Special precautions are required in order to prevent them

[1] Relative to NaI(Tl)

from interacting with the humidity in the air. Otherwise, the crystal will yellow which will degrade its efficiency significantly.

BGO ($Bi_4Ge_3O_{12}$) is a popular choice for many PET systems. In fact most PET systems built today use BGO as their scintillation material [19,20]. Although the output pulse height from BGO is not nearly as high as that produced by other materials, its high density and large photoelectric fraction more than make up for this shortcoming. The high density of BGO allows thinner crystals to be used for photon detection and therefore reduces the uncertainty in determining the point of interaction within the crystal. This improves the imaging performance of PET systems [21].

The decay time constant of a material is the rate at which the scintillation light from a photon interaction decreases. At very high count-rates or input flux levels, when the decay time constant is large, the crystal may still be producing luminescence from a previous event when another event occurs. This overlapping of scintillation light makes it very difficult to differentiate between events. Scintillators with shorter time constants are therefore better suited for high count rate applications. Certain applications, such as time-of-fight PET, actually require significantly shorter decay time constants. Scintillators like BaF_2 have decay time constants of only 600ps, which make them ideal for this application.

Scintillation crystals provide an efficient method to convert high-energy γ-rays into lower energy photons. However, the energy of these new photons must still be measured and made available to a data acquisition system ready to process thousands of events per second. The photomultiplier tube is the key to this process.

1.2 Photomultiplier Tubes

Photomultiplier Tubes (PMTs) are photon sensing devices that were first developed in the late 1930's [22]. These devices are able to convert light photons into an electrical current proportional to the power of the incident radiation. Today PMTs are the photodetector of choice in gamma cameras and PET scanners. Coupled with scintillator crystals such as those discussed in section 1.1, they are able to detect high-energy gamma rays and X-rays in order to form high quality images, which in turn aid doctors and radiologists in diagnosing pathology. The potential of alternative detectors such as *charged coupled devices* (CCD) and *avalanche photodiodes* (APD) [23,24,25] has been explored. However, none have seriously challenged the overall performance of PMTs.

Photomultiplier tubes are devices that make use of some fundamental physical principles in order to convert and amplify photon radiation into electric charge. The process of converting photon radiation into electric charge can be described by a series of equations. Understanding the development of these fundamental equations not only helps us to understand the inner working of the PMT, but can also give us insight into methods that might take full advantage of the potential of the PMT. The following section will describe the physical construction as well as elucidate the physical concepts that govern the functioning of PMTs.

1.2.1 PMT Structure

The structure of a PMT is relatively simple. It is a small compact device without any moving parts, designed to convert photon energy into electric charge. The photons enter the PMT via a transparent window and are converted by the photocathode into photoelectrons. Then the photoelectrons emitted by the photocathode are accelerated towards the first dynode stage by a large applied electric field. As the photoelectrons collide with the dynode they interact with the dynode material and cause the release of a large number of electrons. As a result, there are an even greater number of photoelectrons exiting the dynode than there were entering it. This charge multiplication is repeated with each successive dynode stage until the photoelectron cloud reaches the anode that collects the charge for the tube readout electronics.

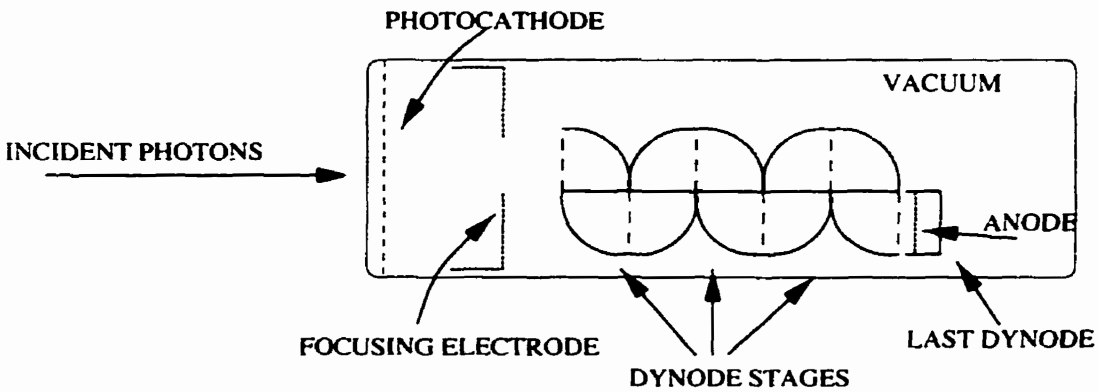

Figure 2 Cross section of a photomultiplier.

The photoelectrons generated by the photocathode are accelerated by a potential voltage towards the first in a series of dynode stages. This high potential voltage is applied between the photocathode and the anode. The voltage can range between 1000VDC and 3000VDC [12] depending on the type of PMT and the particular application. The dynode stages are set to some fraction of the voltage separating the anode and the photocathode. In order to accelerate as many photoelectrons from the preceding stage towards the next one, each dynode is kept at a higher potential voltage than the previous stage. This is most simply accomplished by using a dynode resistor chain as shown in Figure 3. A chain of equal valued resistors creates a constant drop in potential between adjacent resistor nodes. All dynodes are electrically tied to the appropriate resistor chain node creating a constant increase in dynode potential voltage.

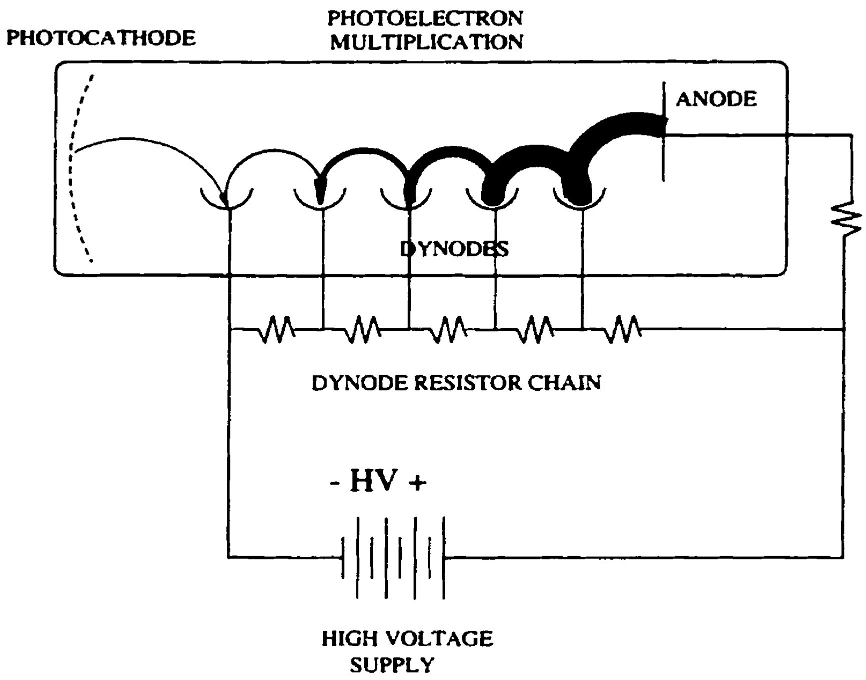

Figure 3 Diagram showing photoelectron multiplication and high voltage dynode resistor chain circuit.

Dynode stages are designed to increase the photoelectron charge by a certain factor and direct the resulting charge towards the next dynode. As the charge is multiplied by successive identical dynode stages, the PMT can achieve a surprisingly high gain. Defining the gain of the i^{th} dynode stage, as δ_i

$$\delta_i \equiv \frac{n_S}{n_P} \tag{8}$$

where n_P is the number of primary photoelectrons reaching the dynode, and n_S is the number of secondary electrons produced as a result of the dynode stage. This gain is determined by the interdynode voltage (V) and by the dynode material and geometry, which set the value of κ. Typical dynode material and configurations result in κ's between 0.7 and 0.8 [12].

$$\delta_i = A \cdot V_i^{\kappa} \tag{9}$$

A PMT with N dynode stages will have a gain (G) of,

$$G = \prod_{i=1}^{N} \delta_i = \prod_{i=1}^{N} \left(A \cdot V_i^{\kappa}\right) = \left(A \cdot V_i^{\kappa}\right)^N \tag{10}$$

If the high voltage is divided equally between all of the dynodes, the gain becomes,

$$G = \frac{A}{(n+1)^{\kappa \cdot N}} \cdot V_{HT}^{\kappa \cdot N} = K \cdot V_{HT}^{\kappa \cdot N} \tag{11}$$

where K is a constant and V_{HT} is the high voltage applied to the tube. Typical general purpose PMTs have 8 to 12 stages [11,12]. PMT gain is therefore very sensitive to fluctuations of the high voltage. High voltage supply settings ranging from 800VDC to 1300VDC can result in an overall PMT gain of ~10^6.

1.2.2 Photoemission

PMT functioning relies on the photoelectric effect. Photons entering the PMT strike the photocathode material, are then absorbed, and as a consequence release a number of electrons. Photocathode materials are specifically chosen for their particular work function (ϕ) characteristics. Materials possessing lower valued work functions allow photons with longer wavelengths, and therefore lower energies, to excite electrons and permit them to escape. A PMT with a lower work function can therefore detect much lower energy photons.

Photoemission can be divided into three main subprocesses:

- Photon absorption.
- Electron diffusion.
- Electron escape.

The first of these, photon absorption, describes the initial interaction between the incident photon and the photocathode material. The flux absorbed $\Phi_P(\nu,x)$ at a particular distance, x from the surface of the photocathode can be described by

$$\frac{d\Phi_P(\nu,x)}{dx} = -\alpha(\nu)\cdot\Gamma(x)\cdot\Phi_P(\nu,x) \tag{12}$$

where $\alpha(\nu)$ is the absorption coefficient of the photocathode material (typically ~$10^4 cm^{-1}$ [15]) and $\Gamma(x)$ is a function which describes the effects of reflection and transmission at the boundaries of the photocathode. For thicker photocathodes $\Gamma(x)\rightarrow 1$ and absorption follows an exponential law:

$$\Phi_P(\nu, x) = \Phi_P(\nu, 0)\left[1 - r(\nu)\right]e^{-\alpha(\nu)x} \tag{13}$$

where $\Phi_P(\nu,0)$ is the incident flux on the surface of the photocathode and $r(\nu)$ is the reflection coefficient at the input surface. As the photons interact with the photocathode material, a portion of the photon energy causes photoelectron generation. The creation of photoelectrons is proportional to the decrease in flux ($\Phi_P(\nu)$) such that,

$$\frac{dn}{dx} = -\alpha_e \frac{d\Phi_P(\nu, x)}{dx} \tag{14}$$

where n is the total number of photoelectrons generated and α_e is the fraction of absorbed photons which excite electrons.

According to equation(14), thicker photocathodes have a far greater probability of photoelectron creation. However, once the photons have been absorbed, the emitted photoelectrons must have sufficient energy to diffuse through the material and still have enough energy to escape from the surface of the material to the vacuum. As photoelectrons diffuse across the photocathode material to the surface of the vacuum, they are vulnerable to interactions with other free electrons. These interactions will decrease the overall energy available to the photoelectrons and make it difficult for them to escape. In metals, there are many electrons in the conduction band. Interactions with "free" electrons occur frequently and cause a loss of energy. For metals, typical escape depths are limited to a few angstroms (~10^{-10}m) [11]. However, in semiconductors the conduction band is virtually empty. This permits electrons to travel greater distances between interactions. Escape depths in semiconductors are typically tens of microns (~10^{-7}m) [26,27].

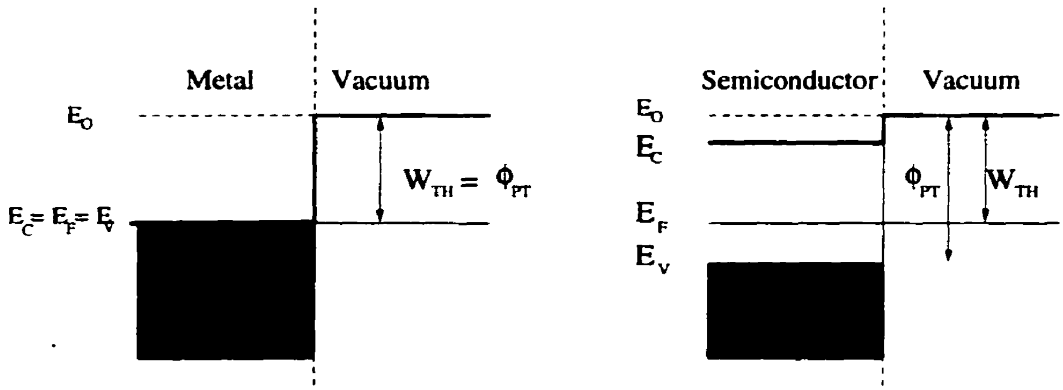

Figure 4 Valence level comparison between metals and semiconductors.

Finally, electrons at the surface of the vacuum must have sufficient energy to cross the surface barrier. This work function is dependent on the material type. Figure 4 compares the conduction bands of metals and semiconductors. In order to be able to escape and reach the vacuum, the photoelectron must have a minimum threshold of energy (ϕ_{PT}). Figure 4 shows that for metals the thermionic work function (ϕ) and the work function are identical.

$$\phi_{PT} = \phi = E_0 - E_F \tag{15}$$

The incident photons must impart sufficient energy to the electrons in order to overcome the potential barrier. This will happen only for frequencies that satisfy

$\nu \geq \frac{\phi_{PT}}{h}$. For typical metals the work function is greater than 3 eV, whereas alkali metals as a group have lower thresholds (~2 eV) [15].

Semiconductors must overcome an even greater barrier. The photoemission threshold is defined by equation (16).

$$\phi_{PT} = E_0 - E_V > W_{TH} \tag{16}$$

Potential barriers of this kind are in the 5-6 eV range, which implies that only wavelengths shorter than ~300 nm can be detected. However, using semiconductor materials that are p-doped can reduce the energy threshold to ~1 eV [15].

1.2.3 Secondary Emission

Secondary emission of electrons is very similar to the photoemission process described earlier with the notable difference that now electrons instead of photons are exciting other electrons in thermal equilibrium into a vacuum. Like photoemission, secondary emission can also be broken down into three main subtopics:

- Primary electrons absorption.
- Electron diffusion.
- Secondary electron escape.

As with the photocathode, the thicker the dynode material the greater the likelihood of the primary electrons exciting secondary electrons. However, the greater the depth at which this occurs from the material surface the more likely these secondary electrons are to lose energy through electron-electron scattering.

Only secondary electrons with energy that is high enough to overcome the potential barrier at the surface of the material can reach the vacuum.

The average depth R, at which a primary electron will penetrate in commonly used dynode materials before interacting has been found to vary as:

$$R = \frac{1.5 \times 10^{-5}}{\rho} E_P^{1.35} \tag{17}$$

where R is the penetration depth (cm), ρ is the material density (g/cm^3) and E_P is the energy of the primary electron (keV) [15]. The loss of energy in primary electrons has also been approximated for energies less than 10 keV to be

$$\frac{d}{dx} E = -\frac{E_P}{R} \tag{18}$$

The loss of energy dE/dx is proportional to the number of secondary electrons n_S created.

$$\frac{dn_S}{dx} = \frac{1}{\varepsilon} \left| \frac{dE}{dx} \right| \tag{19}$$

Combining equation(17) and equation(18) we have

$$\frac{dn_S}{dx} = \frac{1}{\varepsilon} \cdot \frac{E_P}{R} \tag{20}$$

where n_S is the number of free secondary electrons, ε is the average energy required to generate a single electron-hole pair. The closer the free electrons are to the vacuum surface the greater their probability of escape. However, the higher the initial energy of the primary electron the greater the depth of interaction and the greater the number of free electrons produced. This implies that at low primary electron energies there will be low secondary emission ratio (δ) which will increase with E_P to a certain optimal energy, after which the ratio will steadily decrease. Similar to photocathode materials, semiconductors have a marked advantage over metals because of the relatively long mean free path of electrons in the conduction band.

1.2.4 Anode

The role of the anode is to collect the impinging electron cloud as efficiently and as distortion free as possible. In its simplest form, the anode is a collector of all of the charge disseminated by the cathode and each of the successive dynode stages. It must faithfully transfer the resulting signal to the tube readout electronics. The anode must be capable of producing a signal that is proportional to the charge deposited on the anode regardless of the photoelectron rate.

1.2.5 Position Sensitive Photomultiplier Tubes

General-purpose PMTs have a single anode collector and so can only provide an aggregate signal of all of the impinging photoelectrons. The tube cannot identify the actual location of the photon interaction with the photocathode. In fact, great effort is put into the design of PMTs to ensure that the anode signal is independent of the originating point on the photocathode [15]. While this is adequate for many applications, the desire for higher resolution photon imaging necessitated the development of new photodetector types. Efforts were made to modify existing PMT designs to allow them to distinguish photocathode interaction locations across the photocathode [28,29]. Adding multiple small anodes within an essentially normal PMT improved the spatial resolution dramatically while still maintaining the high energy resolution of standard PMTs. Consequently, a specialized category of PMT was developed capable of locating the point of interaction of the photon on the photocathode.

Position-sensitive photomultiplier tubes (PS-PMTs) as they became known, are very similar to their general-purpose PMT cousins. They possess essentially the same structure: a photocathode, several dynode amplification stages, and an anode stage. The main difference is in the construction of that anode stage. Instead of the simple anode collector, PS-PMTs are constructed using complex anodes with several independent outputs which carry information about the photon interaction location on the photocathode.

PS-PMTs rely on the propagation of the photoelectron cloud through the dynodes in a narrow column from the photocathode interaction location to the portion of the anode directly below it. Careful internal PMT electric field design can maintain a tight and constant mapping between the photoelectron original location and the anode charge collection location. The electric field must also be designed such that the propagation delay across the PS-PMT usable surface area is nearly constant.

There are two major categories of PS-PMTs: the crossed-anode wire PS-PMT and the multi-anode PS-PMT. Each anode type has a particular set of advantages and disadvantages associated with it, but all possess the ability to resolve event location within the PMT which general purpose PMTs simply cannot do. Though significantly different from general purpose PMTs, these devices have retained many of the excellent qualities associated with their more standard cousins, namely: high energy resolution, high quantum efficiency and ease of use.

Multi-Anode PS-PMTs

Multi-anode PS-PMTs as their name implies are constructed with multiple anodes, forming a grid. Each anode operates as though it were the singular anode from a general purpose PMT. The charge that each anode captures is from photoelectrons that were generated by a small portion of the photocathode directly above that particular anode. There is an output connection to the outside of the tube for each anode. The anode elements have an isolated impedance matched connection to the readout electronics, which provide an electrical signal that is proportional to the fraction of the photoelectron charge that reaches each individual anode. In this way, the multi-anode PS-PMT creates a grid of signals representing the photon charge reaching the photocathode area directly above each multi-anode element.

The Philips Photonics Company has developed a commercial version of the multi-anode wire PS-PMT: the XP-1700 family of multi-anode tubes. The tubes are constructed with 64 or 96 anodes depending on the model. They use a dynode construction technique that minimizes the cross talk between adjacent anodes. This has been characterized to be less than 10% across adjacent anodes [30,31]. The Philips design uses micro-channels that "funnel" the secondary electrons down to their respective anodes [31]. This method produces phenomenally low cross-talk while still maintaining a high gain ($\sim 10^6$ at 1000v).

Unfortunately, the construction of micro-channel PS-PMTs require a substantial amount of space surrounding the photocathode for structural support of the tube. This large dead space makes it unsuitable for applications that require the direct coupling of scintillation crystals with several PS-PMTs in close formation. Medical imaging applications such as PET and SPECT [32,33] require the very close packing of their scintillation crystals which in general make it impossible to directly couple the crystals to the multi-anode wire PS-PMT. However, as will be discussed in section §2.1, successful designs based on the use of light pipes and multi-anode wire PS-PMTs have been developed [30,34].

The complexity of the readout of the relatively large number of outputs from a multi-anode wire PS-PMT can be reduced substantially. Making use of a passive centroiding circuit, as few as four analog outputs are required [31,35]. In addition, the inter-anode gain variations of the PS-PMT can be minimized by the use of a software lookup map [30]. Although multi-anode wire PS-PMTs remain relatively costly when compared to their single anode counterparts, some have pointed out that the cost per anode can be considered to be quite modest [31].

Crossed Anode Wire PS-PMTs

A second variety of PS-PMTs is the crossed anode wire PS-PMT. This detector type is based on commonly found PMTs with a highly modified anode structure. In order to provide the spatial coordinates of the electron cloud, the anode is made up of several wires extending in the x and y-axes. Figure 5 shows a view of the Hamamatsu R-3941 crossed anode PS-PMT anode structure [36]. A series of anode wires extend across the x-axis of the PS-PMT with a pitch of 3.75 mm while a similar series of anode wires extend across the y-axis with a pitch of 3.70 mm. The anodes from each axis provide a profile of the electron cloud produced by the photon interaction with the photocathode. A centroiding readout approach is commonly applied to this type of PS-PMT. Using a resistor chain, the centroid of the charge distribution for each axis can be determined with only two readout channels per axis.

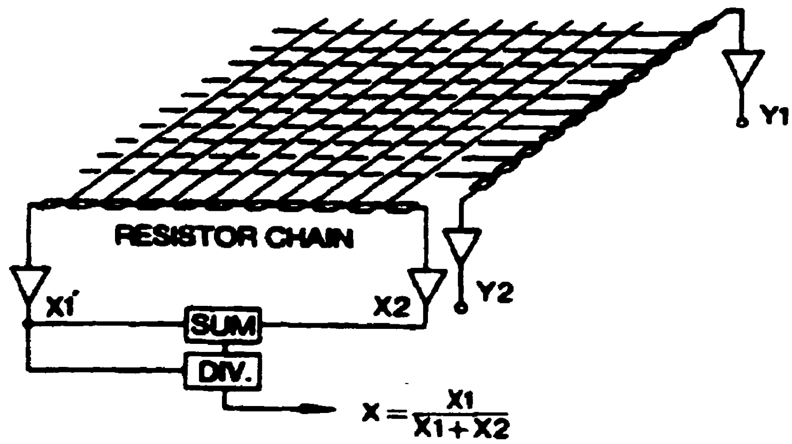

Figure 5 Diagram representing the anode structure from a Hamamatsu R-3941 crossed anode wire PS-PMT [36]. The anode resistor chain for both the x and y-axes can be seen as well as the positioning equation.

The major drawback of the crossed anode wire PS-PMT is the high signal cross-talk between anode wires. The charge spread from one 511 keV gamma ray interaction with a scintillator crystal has been found to span more than 8 of the 18 x-axis anode wires of a Hamamatsu PS-PMT [37,38,39]. However, the distribution of the electron charge has also been characterized as highly Gaussian in form [37,40]. This explains in part the excellent spatial resolution achieved in the central portion of the photocathode using crossed anode wire PS-PMTs with an anode resistor chain readout.

Crossed-anode wire PS-PMTs have greater inter anode cross talk than multi-anode PS-PMTs because of their dynode structure. Multi-anode PS-PMTs such as the Philips XP-1722 use a compact multi-channel dynode [27]. This type of dynode "funnels" the electrons very efficiently and directly towards the anode array. However, the main disadvantage of this type of dynode is that only a small usable area surrounded by a relatively large dead space can be constructed. Crossed anode wire PS-PMTs such as the Hamamatsu R-3941 [11,36] on the other hand use a more open "venetian blind" style of dynode construction. This style of dynode has significant inter anode wire cross talk. However, larger photocathode areas with relatively little surrounding dead space are possible.

The Hamamatsu R-3941 crossed anode wire PS-PMT is a 73 mm×73 mm detector with 18 x-axis anodes and 16 y-axis anodes. It has an effective photocathode area of 60 mm×55 mm [36,41,42]. This gives the PS-PMT a very high packing ratio which makes it suitable for direct coupling to scintillation crystal in a tight imaging formation of the sort used in PET imaging [33,34,43].

1.3 Summary

Gamma ray detection is an integral part of many medical imaging devices as well as many astronomical observation stations. It can be seen that the combination of the high density and high photoelectric fraction of certain crystal types such as NaI(Tl), BGO and LSO when combined with photomultiplier tubes function together with remarkable efficiently in order to convert high energy photons into an electrical signal which can be recorded by standard data acquisition techniques.

New crystal scintillators with remarkable properties are becoming available. Scintillators with light level outputs that were never thought possible are being discovered. New crystal surface treatments are maximizing the light throughput of the crystal. Similarly, PMT research is producing better photocathodes and dynode materials. New position sensitive PMTs with lower cross-talk and higher packing fractions are being developed.

PMTs are excellent low energy photodetectors. They lend themselves to a remarkable number of applications. The simplicity of their design has allowed researchers to develop new PMT crystal combinations, light sharing, PS-PMTs to create remarkable detectors. As will be seen in the following chapters, the development of various block detectors and position sensitive PMTs make them ideal for applications in diverse fields.

POSITION SENSITIVE PHOTOMULTIPLIER TUBE BASED GAMMA-RAY BLOCK DETECTORS

Standard photomultiplier tubes used in PET scanners are typically arranged in functional groups of several PMTs sharing light from a scintillation crystal array [44,45,46,47]. An algorithm is then applied to the resulting signals from the PMTs in order to determine the particular crystal with which the gamma ray interacted. These block detector arrangements allow the use of a small number of PMTs to correctly determine the event location from within a much larger number of scintillation crystals.

PS-PMT technology has been successfully applied to the development of new gamma-ray block detectors [43,48]. Due to their higher spatial resolution, PS-PMT based blocks can be coupled to scintillation crystal arrays with very small elements. These block detectors can therefore be used to more accurately determine the gamma-ray interaction location. Section §1.2.5 described crossed anode wire and multi anode wire PS-PMTs. These two types of PS-PMTs possess significantly different characteristics that determine the possible block detector arrangements. This chapter will focus on the development of two PS-PMT based PET block detectors, one using crossed anode wire PS-PMTs and the other using multi-anode PS-PMTs.

2.1 UCLA *micro*PET Detector

A new and innovative block detector has been developed at UCLA for use in their *micro*PET system [34,49]. The *micro*PET system is a dedicated small animal imaging system. Figure 6 shows the gantry of the *micro*PET system. It has a full

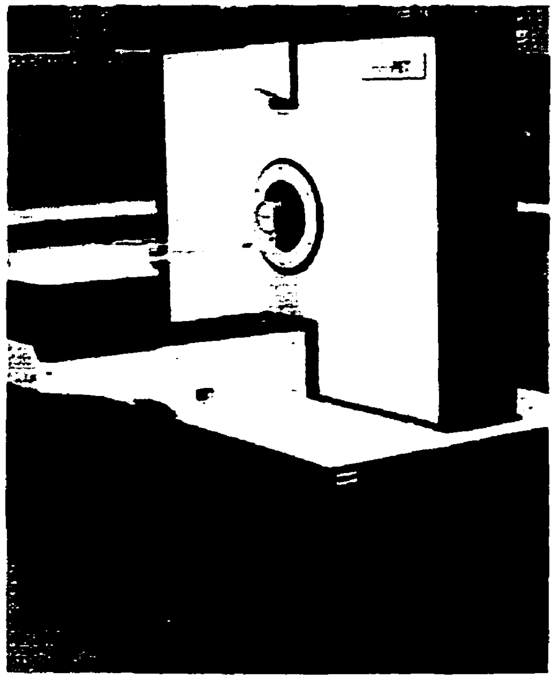

Figure 6 UCLA *micro*PET gantry.

17.2cm diameter ring of LSO scintillation crystals with an opening large enough to allow small primate brain imaging. In order to design the system, they developed an innovative, compact and relatively inexpensive detector.

2.1.1 *Detector Performance Characteristics*

Figure 7 shows the *micro*PET detector configuration. It is based on the Philips XP-1722 multi-channel PS-PMT [31]. This micro-channel plate PMT has extremely low cross talk. Channel neighbours have a cross talk of less than 5% [30], which makes the detector an excellent candidate for very high-resolution measurement applications. The overall signal current gain is comparable to standard PS-PMTs. However, the gain variation from channel to channel on any given device can be as high as a factor of 3:1, and 2:1 between adjacent elements

[30]. Despite this drawback, the excellent cross-talk properties of the tube make it an excellent candidate for PET block detectors.

Figure 7 *micro*PET detector assembly, including a Phillips multi channel PS-PMT, an array of 8×8 LSO crystals connected together by a matrix of fiber optic cable.

One serious problem with the Philips multi-channel PS-PMT in full ring PET block detector configurations is the large dead-space given up in the outer periphery of the tube, which is necessary to maintain structural integrity. A photocathode sensitive area of 33 mm×33 mm combined with a PS-PMT package outer diameter of 80 mm precludes the possibility of directly coupling the scintillation crystal and still maintaining a high packing fraction. In order to overcome this, the UCLA group chose to couple a 64 element, 8 × 8 array scintillator to the Philips tube via a 25cm long array of double clad optical fibers. By coupling the crystal array at a distance, the dead-space surrounding the sensitive area of the tube is no longer a factor constraining the compactness of the scintillation crystal ring.

The major disadvantage of using optical fiber is that the crystal-fiber optical coupling is very inefficient. Much of the scintillation light is lost at the entrance of the fiber. Only approximately 30% of the scintillation light produced actually reaches the photocathode [34]. To overcome this problem, designers upgraded the original BGO based scintillator to an LSO based crystal block, which produces more than 10 times the amount of light per event.

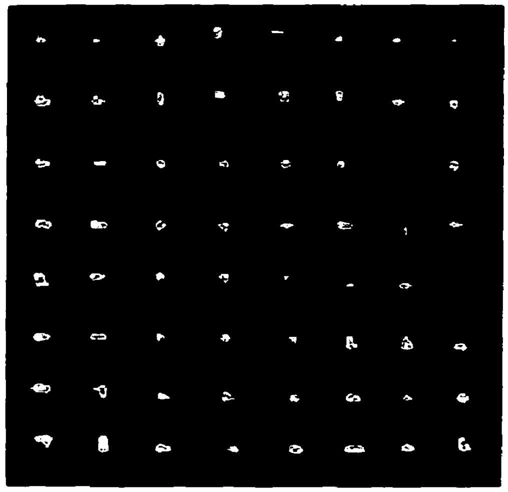

Figure 8 *Micro*PET detector flood source response.

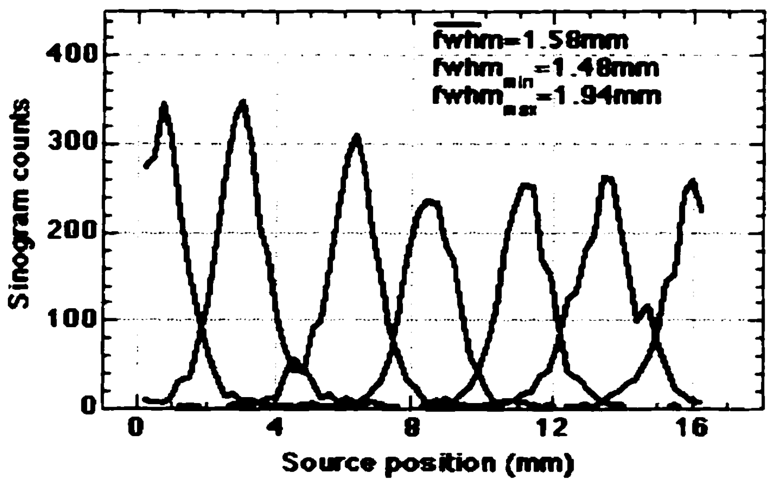

Figure 9 Coincidence results between two microPET detectors.

The Philips XP-1722 provides an 8×8 array of anode outputs. These could be digitized individually. However, the cost would be prohibitive. Instead, the UCLA group has opted for a charge division readout scheme [34].

The final block detector's performance is impressive. Figure 8 shows the very low cross-talk between adjacent anode elements of the Philips XP-1722. Even with the loss of light due to the 250 mm length of fiber optic cable between the LSO crystals and the multi-anode PS-PMT, the energy resolution is still 35%. Similarly, as can be seen in Figure 9, the FWHM for coincidence measurements between two *micro*PET detectors is only 1.58 mm.

2.1.2 Summary

The UCLA microPET block detector made use of the Phillips XP-1722 multi-anode PS-PMTs. By coupling the crystal array to the PS-PMT via some 25cm fiber optic cables, designers were able to use several block detectors in order to form a very tight ring suitable for imaging small animals.

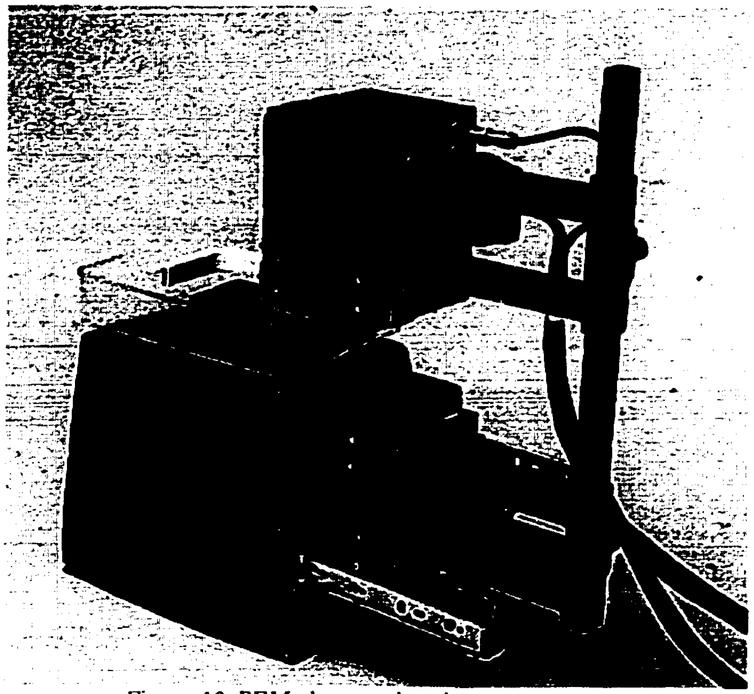

Figure 10 PEM detector housing arrangement showing a modified mammography magnification stage, with two PEM block detectors.

2.2 MNI-PEM Detector

Our team, led by Dr. C. J. Thompson, has experimented with BGO block detectors for use in *positron emission mammography* (PEM). The *Montreal Neurological Institute* PEM (MNI-PEM) project was developed in an effort to create a low-cost dedicated positron emission imaging system to be used in conjunction with conventional x-ray mammography techniques. The work described in this thesis is based on research carried out while developing block detectors used for the MNI-PEM project.

The functional images from a PET-like system such as the MNI-PEM system with injected FDG have been shown capable of easily identifying tumors with diameters of 10 mm [50]. These images can be used to monitor the progress of chemotherapy, or to determine the success of a surgical procedure to remove cancerous tissue. However, the initial motivation for developing the MNI-PEM system was to aid in the early detection of cancerous breast lesions.

Traditional x-ray mammography offers a spatial resolution significantly higher than that found in any other imaging modality used in cancer detection. However, it suffers from a high rate of false-positive detection. This leads to a large number of unnecessary needle biopsy procedures in order to verify the state of the breast mass. The PEM project hopes to reduce the number of unnecessary biopsy procedures by applying the functional information gained toward differentiating between benign and cancerous masses in the breast.

2.2.1 Detector Configuration

The MNI-PEM scanner is designed for use in conjunction with a regular x-ray mammography system. Both an x-ray mammogram and a PEM scan are performed during the same session. Figure 10 shows the original MNI-PEM prototype scanner. This unit consists of two block detectors placed directly opposite one another. The lower detector is placed under the breast inside the x-ray mammography magnification box (seen in Figure 10), while the upper detector is just above the upper breast-compression plate. In this way, the MNI-PEM image can easily be co-registered with the mammogram.

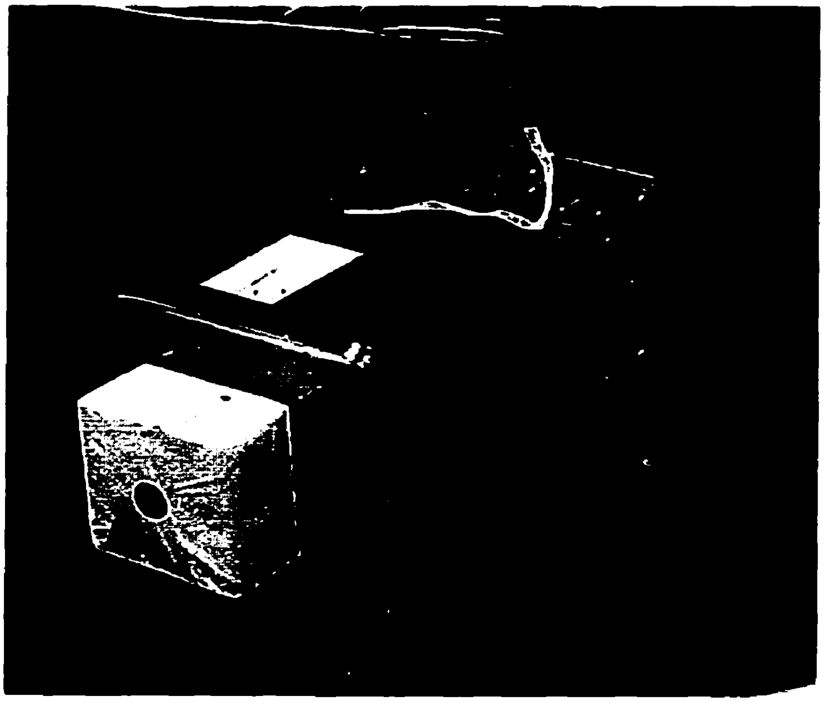

Figure 11 MNI-PEM block detector composed of a Hamamatsu R-3941 crossed anode wire PS-PMT coupled to a Teflon-wrapped BGO scintillation crystal. The figure shows only one of four BGO crystals attached coupled to the PS-PMT.

Each detector is composed of four pixellated 36 mm×36 mm×20 mm BGO blocks optically coupled to a Hamamatsu R-3941 crossed anode wire PS-PMT. Figure 11 shows a detector coupled to a single Teflon-wrapped BGO scintillation crystal block in the center of the photocathode. The location of the gamma-ray interaction is determined using an Anger logic readout which will be discussed in more detail in section §3.2.1.

The MNI-PEM detectors use a novel scintillator crystal arrangement. Instead of being composed of a large array of small BGO crystals individually polished and wrapped in Teflon, the MNI-PEM detectors use large solid blocks of BGO (36 mm×36 mm×20 mm) which are then partially cut into small elements

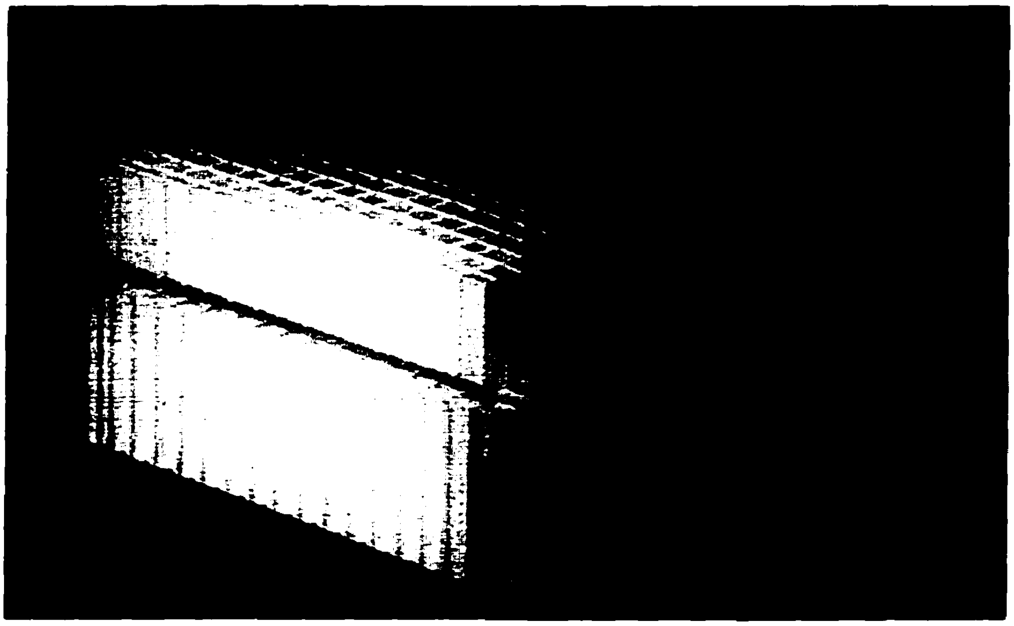

Figure 12 Cut block of BGO used with the MNI-PEM scanner.

interconnected at the center of the block. Figure 12 shows one such BGO block with partial cuts in both the x direction and the y direction only cutting 7.5 mm deep on the top side (closest to the breast) of the block and 11.5 mm on the bottom side (closest to the PS-PMT) of the block. The depth of the cuts are offset in order to maintain an equal probability of 511 keV interaction with the top and bottom sides of the BGO block [2].

The cuts were made on 2 mm centers in both the x-axis and y-axis, creating 1.9 mm×1.9 mm crystal elements with a 0.1 mm separation between the elements. The MNI-PEM BGO blocks were cut such as to offset the top side array and the bottom side array by exactly one half crystal (ie. 1 mm) in each direction. This doubles the effective sampling of the crystals without weakening the structural integrity of the crystal. It also makes it possible to differentiate between near and far crystal event interaction locations, providing depth of interaction information.

After being cut into two offset arrays the block must be etched in order to maximize the light collection efficiency. A special acid mixture was developed [51] to etch away the rough portions of the crystal, leaving behind a smooth polished surface. The whole block is then coated with a white epoxy mixture, which once hardened, plays the dual role of protecting the fragile crystals and of providing optical isolation.

The Hamamatsu R-3941 crossed anode wire PS-PMT tube is a 73×73 mm square tube with 18 x-axis anodes and 16 y-axis anodes. With 12 dynode gain stages and a maximum operating voltage of 1.3kV it has a typical gain of $\sim 10^6$ [12]. The AC coupled last dynode stage provides an early triggering signal for the signal processing electronics.

The R-3941 crossed-anode wire PS-PMT was chosen because of its large field-of-view (60 mm × 55 mm) and relatively small dead space. In order to ensure the success of the MNI-PEM project, the detectors have to be able to image a large portion of the breast, and more importantly be able to capture images very near the chest wall. Multi-anode PS-PMTs such as the Philips XP-1722 used in the *micro*PET have small sensitive photocathode areas with a very large dead space surrounding the photomultiplier tube. Although a fiber optic arrangement allows considerable flexibility in the placement of the scintillation crystals, the resulting loss of light reduces the energy resolution of the detector.

2.2.2 Performance

The combination of small BGO scintillation crystal element size and the spatial resolution of the Hamamatsu R-3941 PS-PMT resulted in the MNI-PEM detectors having a reconstructed resolution of 2.05 mm FWHM [41]. This is far better than the ~4 mm resolution which can be achieved in current PET scanners [52]. A series of three lookup tables are used to determine the efficiency of each crystal element [42]. Using a ^{68}Ge-^{68}Ga flood source the average BGO crystal element energy resolution was found to be 35% [41].

2.3 Summary

The UCLA *micro*PET detector and the MNI-PEM detectors take full advantage of the characteristics of both multi-anode and crossed anode wire PS-PMTs. The low cross talk of the multi-anode PS-PMT make it very adaptable. However, special attention must be paid to the large dead-space surrounding the small active area of the tube. Crossed anode wire PS-PMTs have a much smaller dead-space and a relatively large active photocathode area which makes them excellent candidates for applications which require direct coupling of large scintillation crystals. Unfortunately, the charge from each photocathode event spreads across many anode wires. Both of these PS-PMT styles can therefore be used in order to create high performance block detectors that greatly outperform standard PMT-based PET block detectors. However, great care must be taken when selecting the most appropriate PS-PMT type for a particular application.

Chapter 3

CROSSED-ANODE WIRE POSITION SENSITIVE PHOTOMULTIPLIER TUBE READOUT

Crossed anode wire PS-PMTs have greatly expanded the role of PMTs. They have been found useful in such diverse applications as breast imaging, small animal imaging and gamma ray detectors for nuclear facilities [3,7,49,53]. This is due in part to their compact design, high reliability, and their excellent spatial resolution. Advances such as these were made possible because of the additional information carried by the numerous anodes of a PS-PMT that are not present in standard PMTs. Unfortunately, the large number of anodes in PS-PMTs also increases the amount of data to be captured and processed by the readout electronics. This can require processing the data off-line as well as using a large data storage system.

Standard PMTs with their single anode require at most a single electronic readout channel per photomultiplier tube. PS-PMTs on the other hand typically have from 16 to 96 individual anodes [31]. Having a readout channel for each individual anode would be prohibitively costly. Also, the amount of data to be transferred and processed in order to form an image would be enormous. As a result, PS-PMT readout methods have been developed to preprocess as much of the information coming from the anode wires as possible. This minimizes the cost and complexity of the collection of data without significantly compromising the spatial resolution of the detector.

This chapter will illustrate some of the more common readout methods used for crossed anode wire PS-PMTs as well as describe some recent work which may eventually provide more efficient and accurate positioning results.

3.1 Anode Charge Distribution

Crossed anode wire PS-PMTs ideally should behave just like a close packed array of standard single anode PMTs with their anodes connected together across each axis. This arrangement would result in minimal cross talk between each PMT. However, in reality the electron cloud reaching the anode wires of crossed anode wire PS-PMTs has a pronounced spread across several anode wires. The photoelectric charge captured by anode wires neighbouring the anode wire located under a particular photocathode event is significant. Cross talk in most applications reduces the effectiveness of the detector. However, knowledge of the charge distribution obtained using crossed anode wire PS-PMTs can be used to simplify their readout while maintaining accurate data collection.

Experiments have been carried out attempting to characterize the charge distribution captured by the anode wires of a crossed anode wire PS-PMT [37, 38, 39, 40]. Exposing small optically isolated scintillation crystals coupled to the face of a PS-PMT to a gamma-ray source, the charge from each anode wire was captured and analyzed. As can be seen from Figure 13, the charge spread is symmetrical about the photocathode event location with an approximately Gaussian shape.

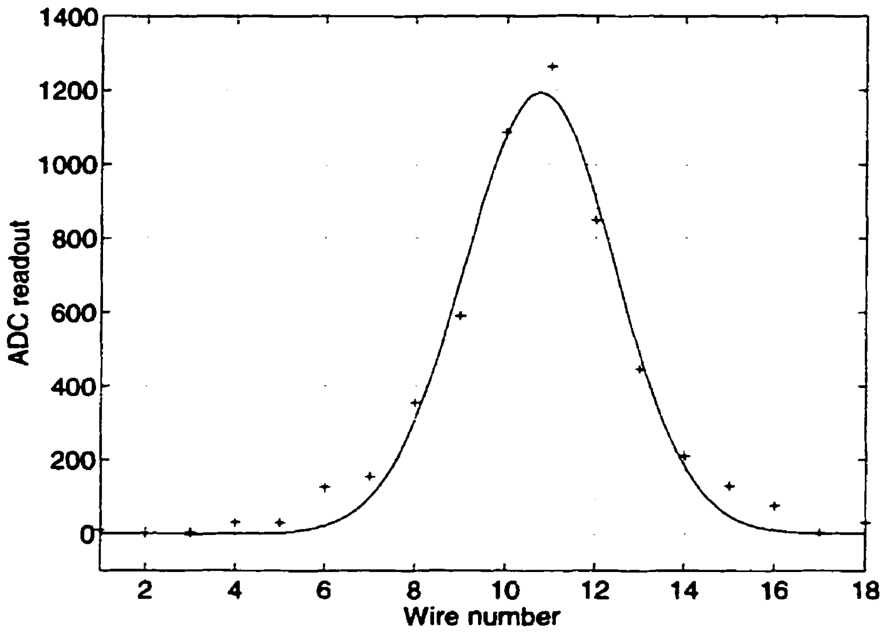

Figure 13 Charge spread distribution captured using a single 3 mm×10 mm×30 mm BGO crystal optically coupled to a Hamamatsu R-3941 PS-PMT. A Gaussian curve with a mean of 10.8 and a standard deviation of 1.67 has been fitted to the captured anode wire charge distribution [37].

Many PS-PMT readout methods have taken advantage of the known charge distribution presented by the many anode wires of the PS-PMT. The photoelectron cloud captured by several anodes can be combined mathematically in order to take advantage of this distribution. Doing so reduces the overall complexity of the readout electronics and simplifies the processing required for imaging applications

3.2 Centroid Based Readouts

The anodes of a crossed anode wire PS-PMT capture a profile of the photoelectric charge reaching each axis. Centroid based readouts take advantage of the symmetrical distribution of charge about the point of origin of the photoelectrons on the photocathode. The charge from each anode wire is used to determine the centroid of charge and hence the point of interaction of the photon with the photocathode.

Centroid based readouts of crossed anode wire PS-PMTs rely on a symmetrical distribution of photoelectric charge across several anode wires and that photoelectric events do not occur concurrently. If these criteria are satisfied, the centroid based readouts provide a very simple and accurate way to acquire position and energy information from photon interactions with the photocathode.

3.2.1 Anger Logic

The first centroid based PMT readouts were developed for gamma cameras in the late 1950's [54]. These γ-ray imaging systems are composed of a large scintillation crystal optically coupled to several PMTs in a close-packed formation. To simplify the readout of the large number of PMTs in the gamma camera, an analog centroiding technique was developed. This technique became known as Anger logic.

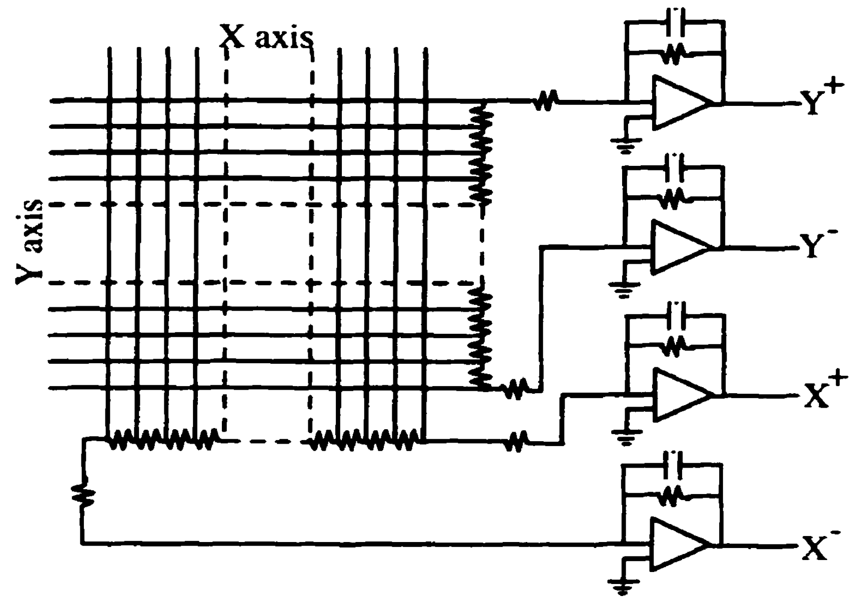

Figure 14 Simplified schematic of a crossed anode wire PS-PMT Anger logic resistor chain readout scheme with charge integrating amplifiers.

Crossed anode wire PS-PMTs can be adapted to take advantage of the simplicity of the Anger logic readout. Like the gamma camera, PS-PMTs have a large number of anodes. The anode wires from each axis can be connected together with an equal valued resistive chain to form an analog centroiding network such as that shown in Figure 14. The four output signals (X^+, X^-, Y^+, Y^-) contain the positioning information and the energy level of the event captured by the PS-PMT. The Cartesian coordinates, X & Y, of the γ-ray interaction are determined using equations (21) and (22),

$$X = \frac{X^+ - X^-}{X^+ + X^- + Y^+ + Y^-} \tag{21}$$

$$Y = \frac{Y^{+} - Y^{-}}{X^{+} + X^{-} + Y^{+} + Y^{-}} \tag{22}$$

while the energy, E of the event is give by equation (23).

$$E = X^{+} + X^{-} + Y^{+} + Y^{-} \tag{23}$$

Anger logic resistor chain readouts greatly simplify the readout of PS-PMTs. A Hamamatsu R-3941 PS-PMT with 18 x-axis anodes and 16 y-axis anodes only requires four analog channels in order to determine the event energy and position. Those four channels produce positioning linearity of events in the central portion of the photocathode that is remarkably high. Spatial resolution of less than 1 mm is typical [55].

Centroid based calculations cannot correctly identify the location of multiple simultaneous events or multiple interaction events (e.g. a Compton interaction followed by a photoelectric event). These events must therefore be discarded. Using analog or software based energy thresholds, unusually high or low energy readings corresponding to multiple overlapping events, or Compton events can be discarded. However, this limits the effectiveness of centroid based readouts at high count rates since a significant portion of γ-ray event must be discarded.

The linearity and accuracy of the Anger logic readout is very high in the central portion of the photocathode. However, at the periphery of the tube the positioning calculation degrades significantly. This is due to the asymmetrical photoelectric charge distribution that results from the truncation of charge that extends beyond the end anode wires. The field-of-view and linearity of Anger logic is therefore reduced. Modified Anger logic readouts have been developed in order to extend the field-of-view and linear region of centroid based crossed anode wire PS-PMT readouts.

3.2.2 Active Segmented Anger Logic

Crossed-anode PS-PMTs using Anger logic type readouts as mentioned above have excellent readout linearity in the central portion of the photocathode. However, this linearity quickly degrades for scintillation events located near the periphery of the tube. In many applications such as SPECT imaging, a band of lead obscures a ring of scintillation crystal around the periphery of the detector. This prevents Anger logic edge distortions from degrading the linearity of the readout near the edge of the detector [56]. This approach, though costly in terms of lost scintillator surface area, does make efficient use of the Anger readout since the central portion of the readout has the best linearity. However, for many applications, the loss of detector area is not a practical option. Consequently, several methods have been developed to improve the Anger logic readout.

Nagai and coworkers have implemented a readout technique that creates three readout zones within the same crossed anode wire PS-PMT [57]. One zone is in the central portion of the photocathode while the peripheral areas make up the other two zones. They have found that more efficient centroid readouts are obtained by treating the readouts in each zone differently. The positioning and energy information are weighted and summed to produce a more accurate and distortion free result across a large portion of the photocathode.

As can be seen in Figure 15, this subdividing of the photocathode is obtained by reading out the photoelectric charge with a modified Anger logic readout. The anodes from each axis are connected together via an equal valued resistor chain, just as in the standard Anger logic readout. However, the charge is read out at four locations instead of only reading out the electron charge at each end of the resistor chain. This in effect creates three subregions in the resistive chain, one in the central region and two in the periphery of the tube.

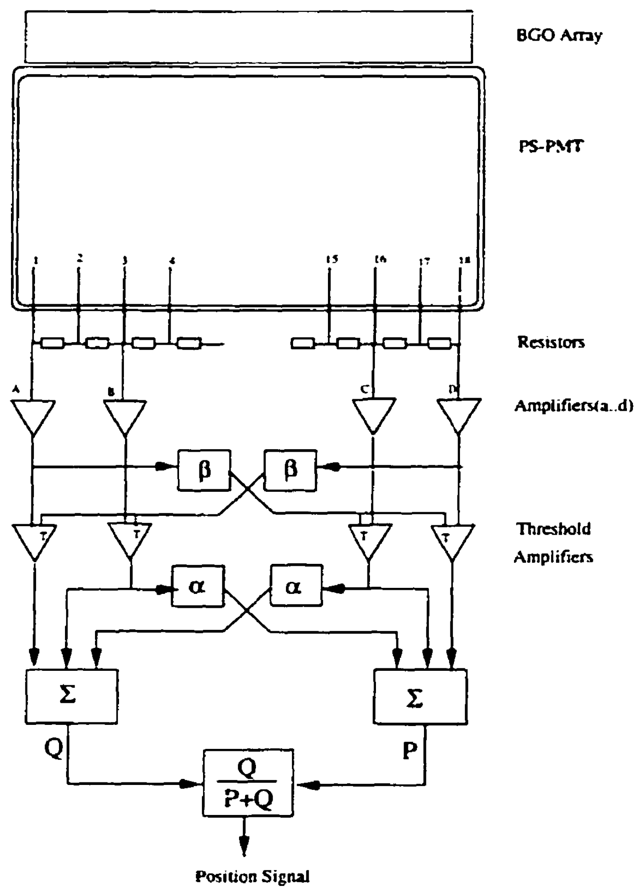

Figure 15 Modified active Anger logic readout technique developed by Naigi and colleagues [57].

The electron charge from the anode resistor chain is processed by the readout electronics shown above schematically in Figure 15. The parameters α and β are chosen empirically (typically between 0.1 and 0.4) [57]. The threshold amplifiers help to eliminate background noise such as PMT dark current. Setting these thresholds takes advantage of the fact that when events are located on one side of the PS-PMT signals coming from the opposite side contain a disproportionate amount of spurious noise that reduces the positioning resolution. Alternatively, at high count rates this system is able to minimize the effect of dual events located on either side of the PS-PMT.

Nagai and colleagues using a Hamamatsu R-3941 crossed anode PS-PMT with a modified Anger readout found a 2.2mm FWHM spatial resolution at the periphery of their photomultiplier tube. The segmented readout is more complex than its Anger logic predecessor. However, it makes up for this complexity by increasing the useful field-of-view of the PS-PMT by 10% without increasing the number of analog channels to be digitized and processed.

3.3 Multi-Channel Based Readouts

Crossed-anode PS-PMTs are typically used with an Anger logic readout in order to minimize the complexity of the readout circuitry. This method yields excellent energy and spatial resolution in the central portion of the PS-PMT. However, the centroid calculation quickly degrades for events near the periphery of the tube. This is because centroid based readout methods such as those described above rely on three assumptions: 1) that the distribution of the photoelectric charge across the anode wires is symmetric; 2) that only photon events produce the charge reaching the anode wires; and 3) that no charge is lost past the end anode wires. These assumptions are only partially valid. Dark current adds charge to each of the anode wires which increases the uncertainty in the determination of the event positioning. Also, the photoelectron charge spread typically reaches more than 6 anode wires [58]. This limits the effectiveness of Anger logic type readouts near the periphery of the tube. Photocathode events located near the edge of the tube will spread charge past the end anode wire, in effect truncating part of the charge distribution. The Anger logic readout becomes non-linear and even double-valued near the edge of the field-of-view. Multi-channel readouts where developed for applications which require high spatial resolution with low position distortion across the entire field-of-view.

Multi-channel readouts capture the charge from each individual anode. That information can then be interpreted in order to take maximum advantage of the information contained in the collected data. Multi-channel readouts are more complicated and require more data processing to determine event positioning than readout methods such as Anger logic. However, they are very flexible and can take advantage of charge distribution models in order to determine more accurately the event position and energy.

3.3.1 University of Southampton Experiments

A group from the University of Southampton [38,40] experimented with new ways to read out the raw data from crossed anode wire PS-PMTs. Their intent was to develop a readout method that maintained the high resolution in the center of the field-of-view of the PS-PMT while at the same time increased the spatial resolution near the edges of the photocathode. They chose to explore the potential of more sophisticated and complex readout methods of crossed-anode wire PS-PMTs.

In a series of experiments the Southampton group examined the spatial and energy resolution of a Hamamatsu R-2487 and R-3292 series crossed-anode PS-PMTs [59,60] using two different readout methods: standard Anger logic, and peak detection using a Gaussian curve fitting algorithm. All of these experiments were carried out using a custom designed charge integrating IC which samples all of the channels simultaneously and then shifts them out serially to be digitized.

In order to explore the potential of a multi-channel readout, an experiment was devised such that the advantages and disadvantages of a peak fitting algorithm could be compared with those of the more standard centroiding method. A 2 mm×2 mm×5 mm NaI(Tl) crystal was coupled to a Hamamatsu R-2487 crossed-anode PS-PMT. A 5.9 keV γ-ray source was used to repeatedly irradiate the crystal while it was optically coupled to the PS-PMT face at various positions along the x-axis of the tube. The linearity of the two readouts was then compared (see Figure 16).

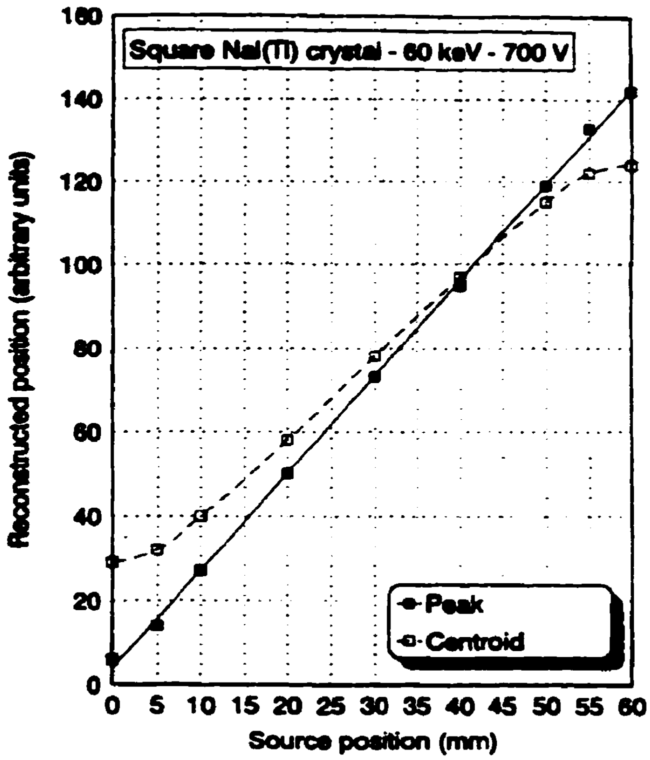

Figure 16 Comparison of the readout linearity of Gaussian peak fitting multi-wire readout and centroid readout [40].

The result of these experiments verified that in the central portion of the PS-PMT the readout linearity for both the centroid and the multi-wire readouts is very similar. However, near the periphery of the tube their performances diverge. As expected, the centroid calculation becomes non-linear as it approaches the edges of the photocathode. Conversely, using the Gaussian peak fitting algorithm, spatial resolution and linearity were maintained throughout the field-of-view of the PS-PMT.

A similar experiment was carried out using a pixelated array of 16 CsI(Tl) crystals (1.25 mm×1.25 mm on 1.30 mm centers). Figure 17 shows the result of a flood irradiation of 122 keV gamma rays using a conventional Anger logic readout, while Figure 18 shows the results of the same experiment carried out with a peak fitting readout algorithm. The readout spatial positioning improved considerably as a result of the Gaussian peak fitting algorithm. The Anger logic method produced a FWHM of 1.3 mm, whereas the Gaussian peak-fitting algorithm achieved a FWHM 0.9 mm, representing a greater than 30% improvement in position calculation.

The University of Southampton's experiments show that significant improvements in crossed anode wire PS-PMT field-of-view and spatial resolution can be achieved using a multi-channel technique. They were able to reduce the complexity of their multi-channel readout system by sampling the data on all of the anode wires and then shifting them serially to a digitizing system. However, by serializing the data stream they reduced the potential throughput of their data acquisition system by a factor of 16, thus minimizing the effectiveness of this method at high count rates.

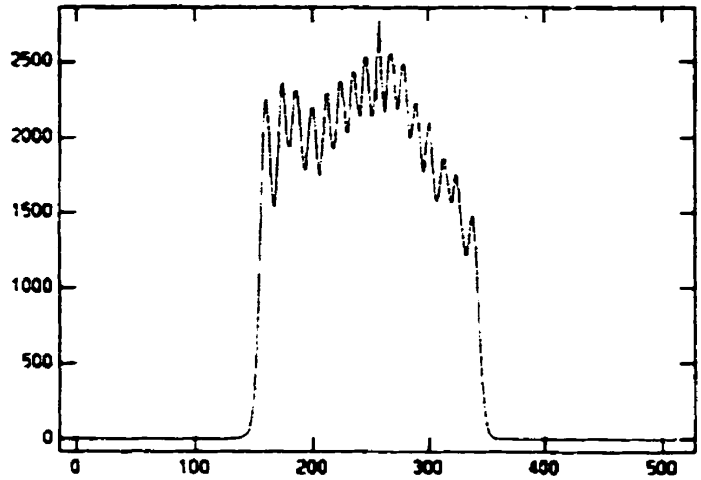

Figure 17 Centroid based readout with a FWHM of 1.3 mm [38].

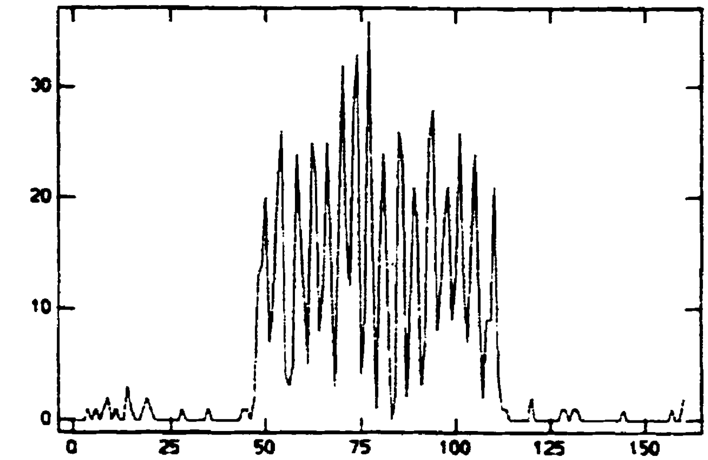

Figure 18 Gaussian peak-fitting readout with a FWHM of 0.9 mm.

3.3.2 A Sparse Targeted Anode Wire Readout

Multi-channel crossed anode wire PS-PMT readouts require a large number of electronic channels and much data processing; however, they also accurately determine the photocathode event location across the entire photocathode. On the other hand, Anger logic readouts provide a very simple means of collecting data, which produces excellent spatial resolution in the central portion of the PS-PMT. Their disadvantage is that they produce much poorer results near the edges of the field-of-view. The sparse targeted response is intended to be a compromise between these two methods. It merges the simplicity and high count rate capabilities of the Anger logic readout with the high spatial resolution and enhanced field-of-view of a multi-channel readout.

The electron distribution across the anodes of a crossed anode PS-PMT has been shown to fall almost entirely on the 6 anode wires nearest the photocathode event on a Hamamatsu R-3941 PS-PMT [39,40,58]. If noise is evenly distributed across all of the anode wires, the signal contribution from the remaining anodes must therefore have a much lower *signal to noise ratio* (SNR). A method was explored by the author to take advantage of this uneven SNR distribution.

Electronic noise and PMT dark current have been shown to be independent of the photocathode event location [12,15]. Since most of the photoelectron charge is captured by only a few anode wires, it is these few wires which contain the majority of the information required to determine the location of the photocathode event. The anode wires located further away from the photoelectron charge distribution center carry some information about the event location. However, they also have a disproportional amount of noise. Using the charge collected by those anode wires in the event location calculation can actually reduce the spatial resolution of the readout.

The sparse targeted readout is designed to select only the small subset of anode wires located directly beneath the photocathode event in order to determine the photocathode event location. This has the benefit of reducing the number of channels to be digitized and the amount of information to be processed significantly. The photocathode event location is determined using the photoelectric charge from the anode wires with the highest SNR. Since the remaining outside anode wires have a low SNR, little photoelectric charge is lost. This increases the spatial resolution of the detector and makes lower energy discrimination levels possible [38].

The data collected by the sparse targeted readout consists of the photoelectric charge collected from the six anode wires nearest to the center of the photocathode event and an address identifying from which anode wires the data was captured. In order to determine the location on the photocathode of the photon interaction, the data is fitted to a Gaussian curve. As discussed in section §3.3.1, Bird and coworkers demonstrated that this yields a spatial resolution improvement of 30% over a conventional centroid calculation [40]. With the additional improvement in the overall SNR due to the sparse targeted readout, an even greater improvement would be expected.

System Design

The sparse targeted readout system was designed for use with a Hamamatsu R-3941 crossed anode PS-PMT with a pixellated BGO scintillation crystal. This PS-PMT has an anode grid of 18 anode wires in the x-axis and 16 anode wires in the y-axis. These detectors are fully described in section §2.2. Figure 19 shows a simplified schematic of the readout system.

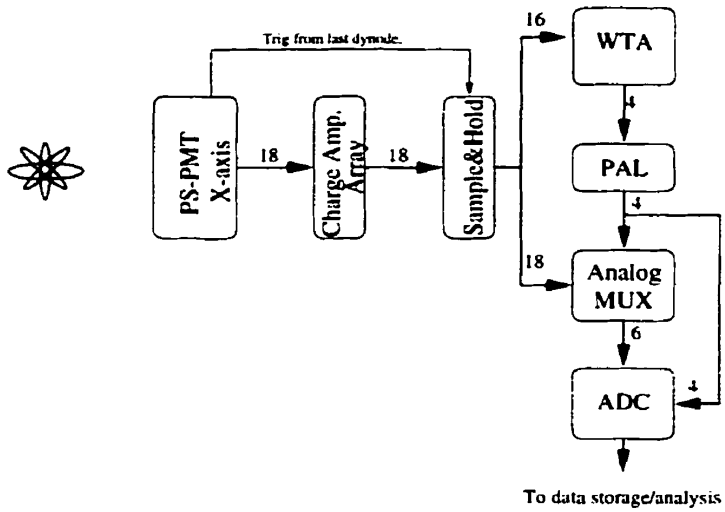

Figure 19 Schematic drawing of the sparse targeted multi-wire readout for crossed anode PS-PMTs. (one axis shown)

The charge from all channels is integrated by a series of amplifiers. The signal from the first dynode is used to trigger a bank of sample-and-hold ICs that latch the peak amplitude of all the channels. The sampled peak values are sent to a *winner-take-all* (WTA) custom-designed integrated circuit. Its purpose is to determine the channel number of the anode wire with the highest amplitude signal. This corresponds to the anode wire nearest the photocathode event. The six anode wire analog signals surrounding the photocathode event location are then directed to a CAMAC based [61] Jorway Aurora14 ADC [62] by a bank of analog multiplexers in order to be digitized along with the information determining the multiplexer settings. A peak fitting calculation is then applied to the data collected from the anode wire subset.

Signal processing

The sparse targeted readout circuit shown in Figure 19 has been designed so that it can operate at very high count rates. Figure 20 shows the timing diagram associated with the sparse targeted readout. The system is designed around an Aurora14 ADC with a conversion rate of 1μs/event (t_{ADC}). The ADC samples the signal immediately and then begins converting the data. This allows the pipelining of the sparse targeted readout design. While the ADC is converting the data, the rest of the system is preparing for the next event. This effectively eliminates most of the conversion time of the ADC.

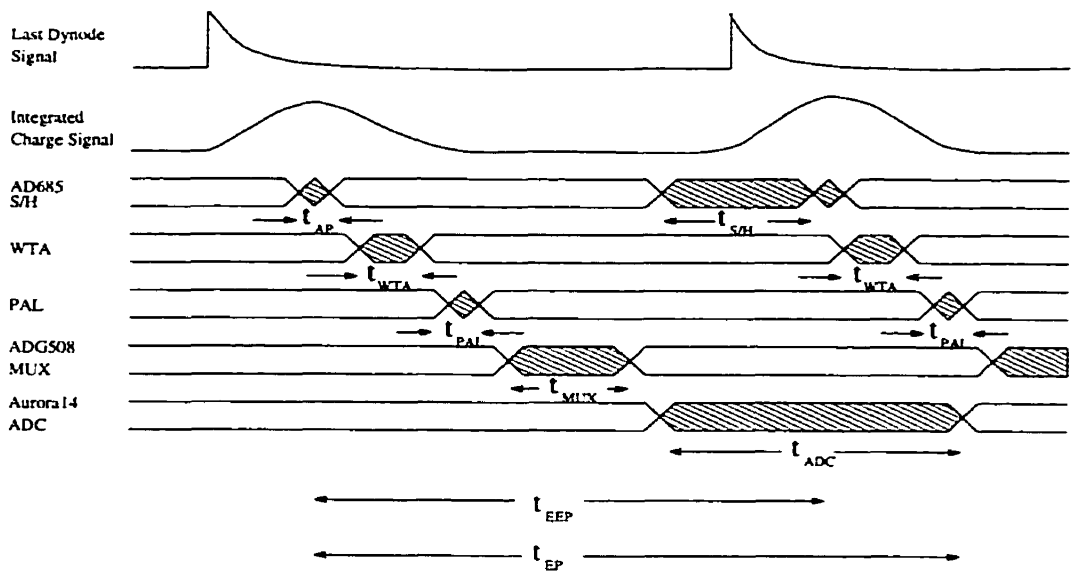

Figure 20 Timing diagram showing the relative timing used for the sparse targeted readout.

The bank of AD685 sample and hold ICs have a fast aperture time (t_{AP}) but must be allowed to sample for 500ns ($t_{S/H}$) before they can be retriggered. The WTA circuit has a propagation delay of 100ns (t_{WTA}) and the PAL (t_{PAL}) and the multiplexer array have a combined delay of 425ns (t_{MUX}). The Aurora14 ADC has a maximum conversion rate of 1μs/event. Together, they account for the total event processing time, t_{EP} which is given by equation(24).

$$t_{EP} = t_{AP} + t_{WTA} + t_{PAL} + t_{MUX} + t_{ADC} = 1.53\mu s$$

(24)

t_{EP} is the time from when the sample is taken until digital data is ready to be sent to the processing system. However, as demonstrated in equation(25),

$$t_{EEP} = t_{AP} + t_{WTA} + t_{PAL} + t_{MUX} + t_{S/H} = 1.03\mu s$$

(25)

pipelining reduces the effective event processing time, t_{EEP} to only 1.03μs. This is only 30ns greater than the Jorway Aurora14 ADC's conversion time, t_{ADC}.

Circuit Block	*Delay*
T_{AP}	2.5ns
T_{WTA}	100ns
T_{PAL}	25ns
T_{MUX}	400ns
T_{ADC}	1.0μs
$T_{S/H}$	500ns

The maximum sustainable data rate given t_{EEP} is 9.7×10^5events/s. Assuming a Poisson distribution and a singles count rate of 10×10^3event/s, a sparse targeted system can gather information from 98.9% of the photocathode events. Even with a singles rate of 100×10^3event/s, the targeted sparse readout can still capture 90.0% of the photon events.

Winner-Take-All

The WTA IC is at the heart of the sparse targeted readout. It determines which anode wire is nearest to the photocathode event. WTA integrated circuits have been used in artificial intelligence neural network research for many years [63,64]. They are designed to make rapid comparisons between several decision nodes and select the most "correct" decision. In analog designs, a voltage represents the likelihood of a particular decision node being correct. The WTA therefore has to rapidly compare a large number of voltages and determine the address corresponding to the node with the highest voltage.

In the sparse targeted readout, a decision must be quickly made about which anode wire channels must be multiplexed and sent to the digitizer. This is a very similar situation to neural network decision making. The signals from the sample-and-hold banks hold the value of the integrated photopeak from all of the anode wires. The location of the peak amplitude signal belongs to the anode wire nearest the event location. The WTA IC needs only to provide the address and the analog multiplexers are able to select the 6 nearest anode wires to be digitized.

WTA ICs are not currently available commercially. We contacted a group at the University of California at Berkeley who had recently developed a WTA circuit for use with a PET block detector [65]. They designed a 16 channel WTA IC capable of resolving the location of a photoelectric peak from the signal resulting from a integrating charge amplifier IC [66]. The Berkeley WTA IC is able to identify the correct channel within 50ns as long as the largest voltage is at least 20mv greater than the next largest channel. Unfortunately, their IC was designed

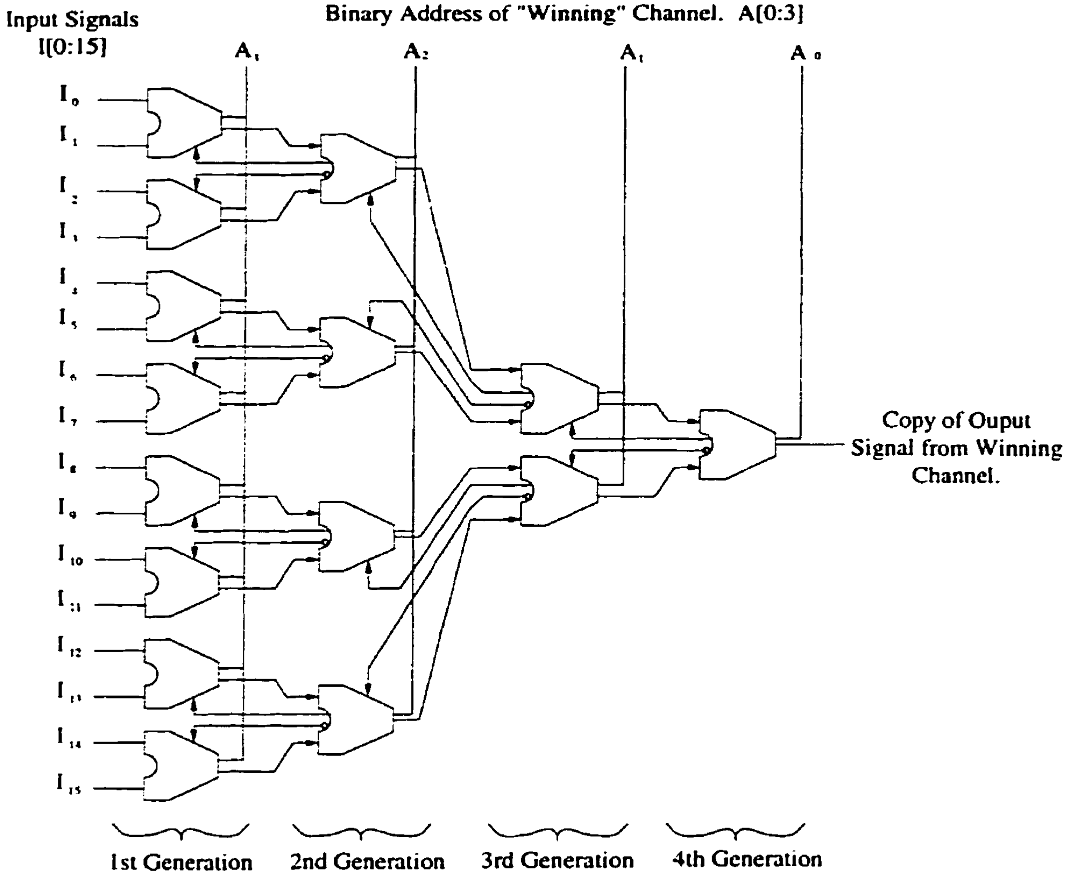

Figure 21 Schematic of the winner-take-all integrated circuit.

for use with a PIN photodiode array and therefore was not easily adaptable for PS-PMT use.

Instead, we chose to develop our own custom WTA IC based on an earlier design by a group from the University of London [67]. This design used a simple system of repeated blocks, cascaded together to form a binary decision tree. Figure 21 shows a 16 channel WTA circuit based on their topology. The entire process is reduced from deciding which of the 16 channels has the highest voltage, to which of two adjacent channels is greater. That analog signal is then passed on via a signal steering device and the next generation of decision making cells compares the new signals to determine which is the greater and then passes it on to the next caparison level. Each level halves the number of channels being considered. This binary decision tree continues until only two channels remain to be compared. The number of decision-making levels required for a certain number of input channels is described by equation(26)

$$n = \log_2 m \tag{26}$$

where *n* is the number of decision levels required and *m* is the number of channels to be considered in the decision.

The x-axis of the R-3941 PS-PMT has 18 anode wires, and according to equation(26) a 5 level WTA circuit is required in order to determine the winner. However, since 6 anode wires nearest the photocathode event center are to be digitized, the WTA was designed to examine only the 16 most central anode wire signals. This simplification resulted in no loss of information given that for events centered over the peripheral anode wires, the WTA would select the neighbouring anode wire as the "winner" and instruct the multiplexer to select the 6 outer most anode wires, including the true winner.

A high performance 14GHz FT bipolar technology[2] was available to us through the *Canadian Microelectronics Corporation* (CMC) [68]. Their service provided a standard tile with a pre-placed array of standard devices. Two metal layers could then be used to interconnect the various devices together in order to form a custom circuit. Full **HSPICE** models were also provided by CMC in order to

[2] Lucent Technologies array: best-1 process.

run circuit simulations with interdevice parasitic parameters included in the models. As part of the service, the final circuit would then be processed with metal-1 and metal-2 layers and then packaged in a 64-pin CLCC[3] package.

The WTA designed by the group from the University of London used a clever arrangement using current based signal processing. Unfortunately, the CMC 14GHz FT technology had lateral pnp transistors with extremely low beta values ($\beta<2$), which made current steering designs impractical. A modified circuit was therefore developed using a voltage rather than current steering approach in order to avoid using pnp transistors in the signal path.

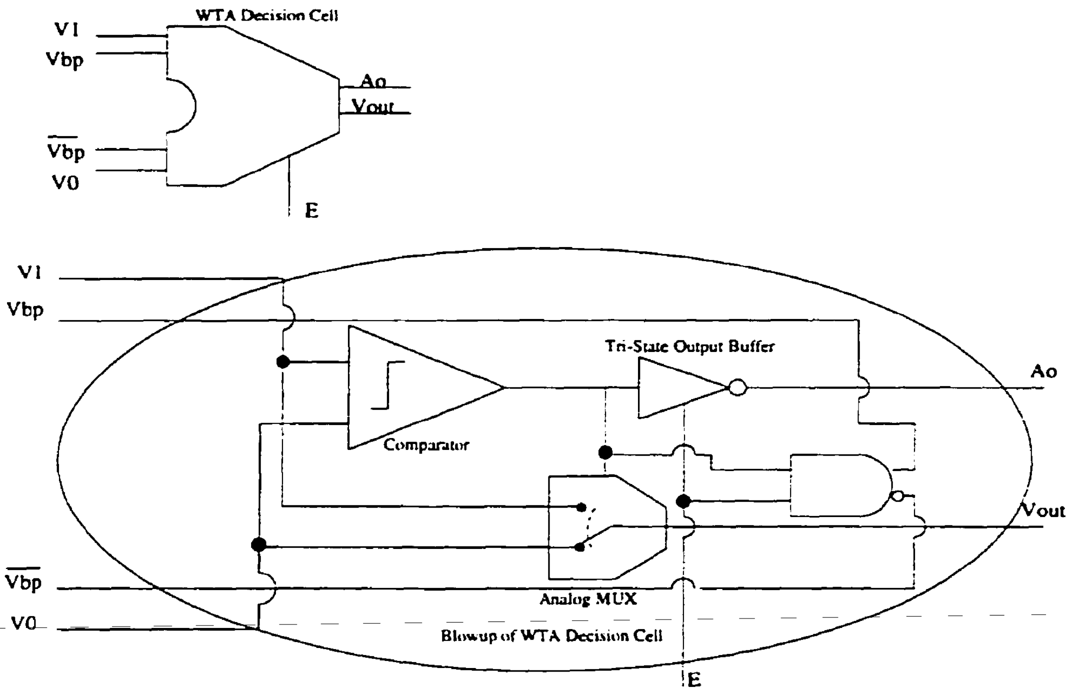

Figure 22 Schematic showing circuit blocks used in WTA decision making cell.

[3] Ceramic leaded chip carrier.

The implementation of the WTA decision cell is shown in Figure 22. It is constructed using only 4 functional circuits: a comparator, a voltage steering circuit, a tri-state buffer and a differential output NAND gate. The comparator circuit is a simple two stage differential npn pair with a gain of 60dB and a resolution of 3 mv. The voltage steering circuit is based on a Gilbert gain cell [69]. It multiplexes the voltage selected by the comparator to the next generation of decision-making cells.

The propagation delay of the WTA IC is determined by the sum of the forward propagation delay (t_{FP}) of the analog copies of the winning signals and the back propagation delay (t_{BP}) of the "pruning" digital signal which enables the outputs of the winning branches in the decision tree. The forward propagation delay is described by equation(27)

$$t_{FP} = n \cdot (t_{comp} + t_{mux}) \tag{27}$$

where t_{comp} is the comparator delay (~8 ns), t_{mux} is the delay due to multiplexer (~12 ns) and n is the number of stages in the WTA IC (n=4). Similarly, the back propagation delay is defined by equation(28)

$$t_{BP} = n \cdot t_{NAND} + t_{TRI} \tag{28}$$

where t_{NAND} is the NAND gate delay (~2 ns) and t_{TRI} is the tri-state buffer delay (~6 ns). The total WTA IC propagation delay is the sum of both equation(27) & equation(28). The propagation delay for the complete four-stage WTA circuit is therefore approximately 94 ns.

Unfortunately, attempts to test the packaged WTA devices proved unsuccessful. Serious faults in the metalization process were found in all of the IC's provided by CMC. Figure 23 and Figure 24 show such fatal faults. As a result the WTA IC design was never verified.

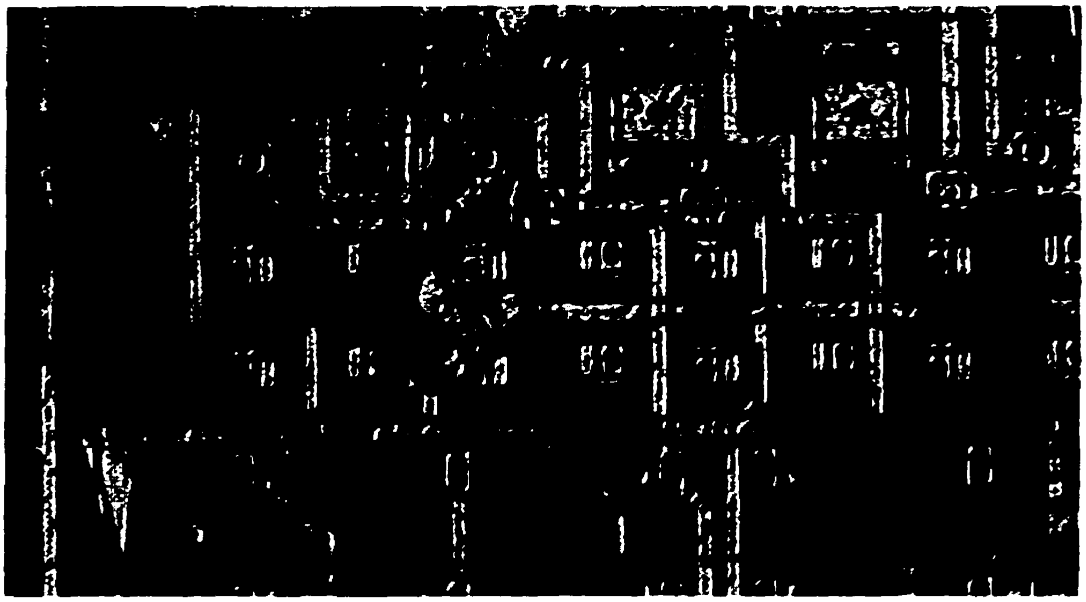

Figure 23 Image showing part of the WTA circuit fabricated through the CMC service. Improper etching of the wafer left the WTA unusable.

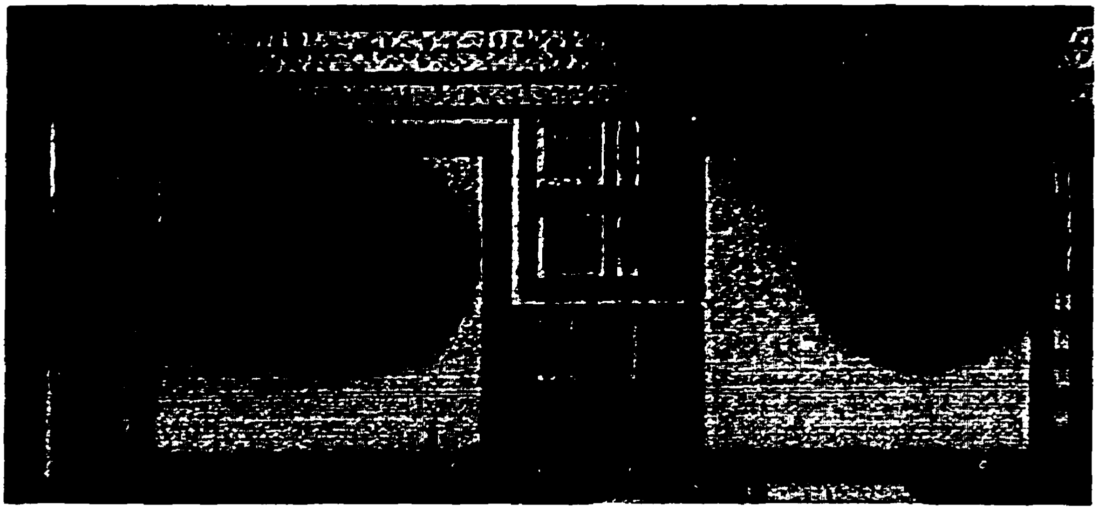

Figure 24 Image of the WTA circuit showing a metal-1 trace with a missing section.

Discussion

The sparse targeted readout project was abandoned shortly after the failure of the WTA IC. This was in part due to budget and time constraints, as well the availability of new inexpensive high performance ADCs [70]. These developments have made it possible to consider implementing an all-digital targeted readout. Fast inexpensive ADCs in conjunction with compact and flexible FPGAs could allow the multi channel readout to be performed quickly and efficiently.

3.4 Summary

Crossed anode wire PS-PMTs have a significant photocathode charge spread. Several readout techniques have been developed in order to maximize the spatial resolution of the detector while minimizing the cost and complexity of the readout.

Anger logic based readouts take advantage of the symmetrical charge distribution reaching the anode wires. By taking the centroid of charge deposition, they achieve very high spatial resolutions in the central portion of the PS-PMT field-of-view. However, the quality of the readout degrades quickly as events approach the edge of the field-of-view.

Multi-channel readouts measure the charge collected by individual anode wires. This information results in a more precise determination of the photocathode event location. They have been shown to have a 30% higher spatial resolution over standard Anger logic readouts. However, the readout electronics associated with these readouts are significantly more complex than Anger logic readouts.

A SIMPLE ANODE RESISTOR CHAIN OPTIMIZATION TECHNIQUE

Position sensitive photomultiplier tubes (PS-PMT) have been used in miniature gamma cameras by Yasillo [71], and in small animal PET scanners by Watanabe [72] and Weber [73]. Typically, the anodes are connected to a resistor chain and the charge from either end of the string is read out in a manner similar to that used in a conventional gamma camera [54]. If the crystal is a solid slab, the light spread in the crystal is significant. However, if the crystal is composed of many optically isolated elements, there is very little light spread in the crystal, and the light collected on the photocathode is concentrated in a portion directly below the crystal. Bird [40] has shown that over 95% of the photoelectrons are collected by only six of the 17 anodes of a Hamamatsu R-2487 PS-PMT when using a 2×2 mm CsI crystal. Similarly, we have shown that 87% of the signal is confined to six wires when using 2×2 mm BGO crystals with a Hamamatsu R-3941 PS-PMT [58]. The standard resistor chain in this PS-PMT has $1\,k\Omega$ resistors between each anode wire. This provides a linear readout of the charge deposition in the central portion of the PS-PMT. However, for events near the periphery of the PS-PMT, the charge spread can extend past the last anode wire [58]. This truncation of the charge distribution causes the position readout to be non-linear near the edges of the PS-PMT. In this chapter, we propose increasing the value of the resistor between the last two anode wires in order to compensate for this lost charge, thus increasing the range of linear readout and the field-of-view of the detector.

4.1 Charge Distribution Model

As discussed in section §3.2, the standard resistor chain readout first developed by Anger [54] used equal valued resistors placed between adjacent gamma camera PMTs. Event positioning was determined by the centroid of charge distribution resulting from the current measured at the ends of the resistor chain (X^+, X^-, Y^+, Y). Equation (29) is the Anger logic equation.

$$X = \frac{X^+ - X^-}{X^+ + X^- + Y^+ + Y^-} \tag{29}$$

When crossed anode wire PS-PMTs were first developed, Anger logic was the natural choice to provide the position readout [74]. Figure 14 shows the standard Anger logic position readout for crossed anode wire PS-PMTs. Anode wires from one axis are all tied together by a resistor chain that is made up of equal valued resistors. The current signals at both ends of the chain are used with equation(29) to determine the event position in the axis. Together, the two resistor chains provide the Cartesian coordinates to locate the event origin on the PS-PMT photocathode.

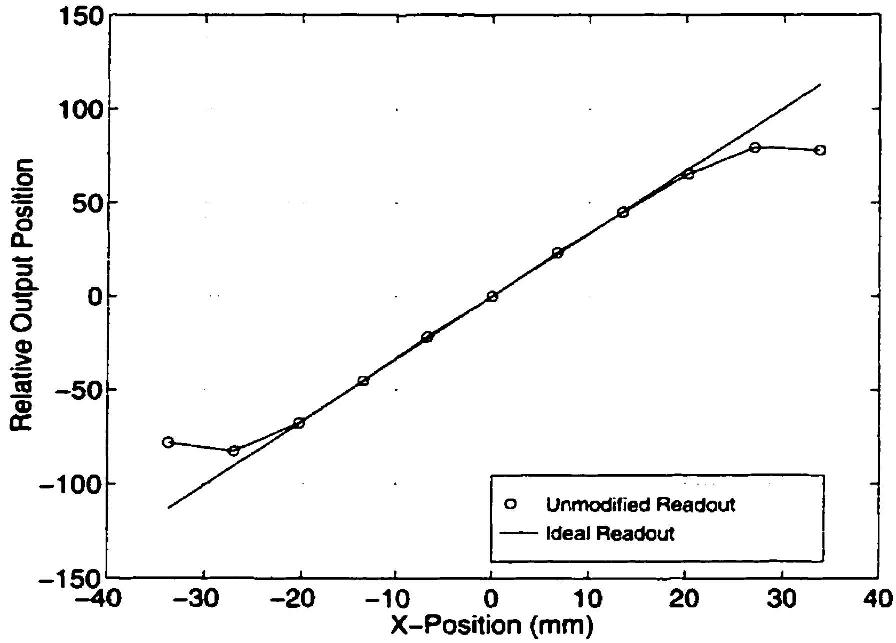

Figure 25 Plot showing the double valued nature of an unmodified resistor chain readout from a Hamamatsu R-3941 PS-PMT using optically isolated BGO crystals.

We have found that when using crossed anode wire PS-PMTs, significant distortion and even double valued positioning can result at the periphery of the tube. Figure 25 shows the actual position readout of an unmodified resistor chain and that of an ideal readout. Although linearity distortions can be compensated with position look-up tables, possible double valued readouts present a greater problem. Since event positioning cannot be uniquely determined for those regions near the edge of the PS-PMT face, they must be discarded, significantly reducing the usable field-of-view.

The simple method presented in this chapter was developed to increase the range of linear readout and to increase the field-of-view of crossed anode wire PS-PMTs. It relies on 3 basic assumptions: that the light spread from the crystals is small, that the charge distribution is symmetric, and that the charge extending past the end anode wires is lost and not "reflected" onto the anode wires.

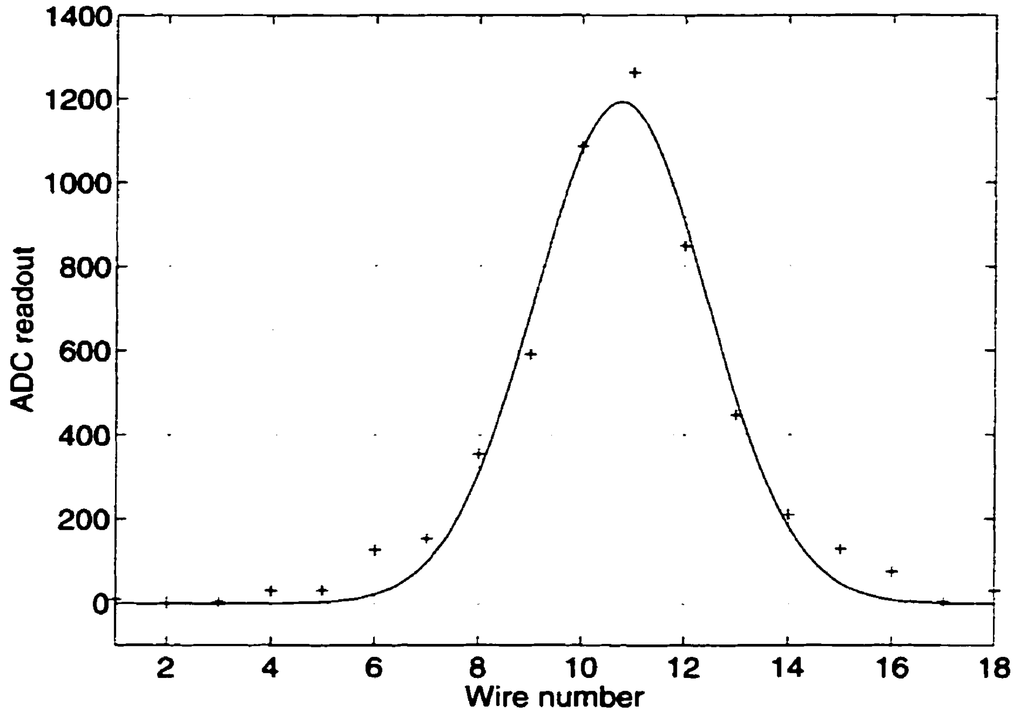

Figure 26 Gaussian charge distribution observed from a 3×10×30 mm optically isolated BGO crystal. Measurements were made using x-axis anode wires of an R-3941 Hamamatsu PS-PMT. Collected data was fitted to a Gaussian curve with $\sigma=1.67$ & $\mu=10.8$.

Using an array of amplifiers to amplify the charge on each anode wire, the average distribution over a large number of events (~10k events) was calculated. We have previously shown [58] that with a single BGO crystal near the center of the field-of-view, the charge spread is limited in extent and can be closely approximated by a Gaussian curve. (see Figure 26). The Gaussian distribution is defined by equation (30),

$$\Gamma(n,\mu)=\frac{1}{\sqrt{2\pi}}e^{\frac{(n-\mu)^2}{2\sigma^2}}$$

(30)

where μ is the mean position of the charge location, which corresponds to the crystal position, σ is the standard deviation of the charge spread and n is the position offset of the n^{th} anode wire. We have also shown in Figure 27 that for crystal elements close to the edge of the field-of-view the Gaussian charge distribution is truncated.

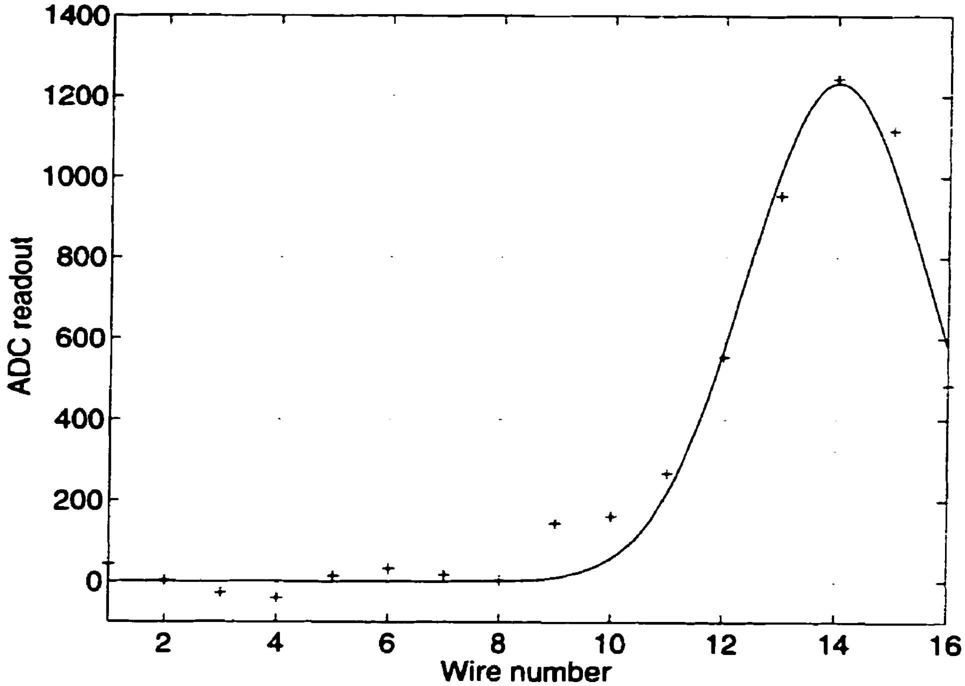

Figure 27 Truncated Gaussian distributions measured by using a 3×10×30 mm optically isolated BGO crystal. Measurements were made using the y-axis anode wires of an R-3941 Hamamatsu PS-PMT. Collected data was fitted to Gaussian curve with σ=1.62 & μ=14.0.

Given that the above assumptions hold, we can modify the resistor chain in order to compensate for the lost charge past the end anodes. Increasing the resistance between both end anode wires and their nearest neighbors has the effect of channeling more current for events near the periphery of the PS-PMT towards that side of the resistor chain. By carefully choosing the value of the resistance, the readout can compensate for charge lost beyond the anode wires.

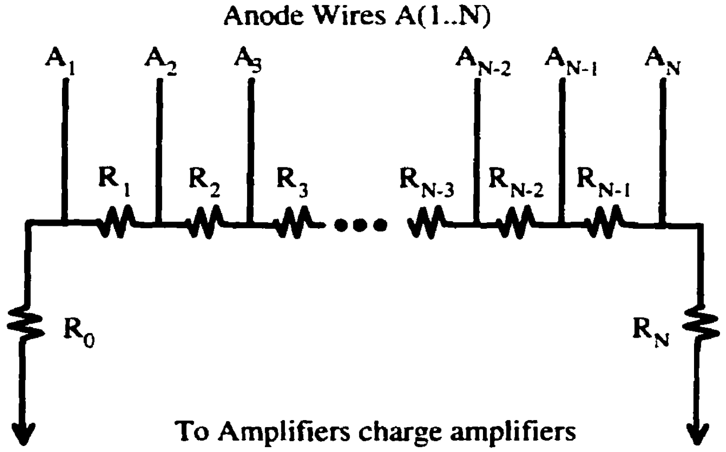

Figure 28 Crossed anode wire PS-PMT resistor chain.

4.2 Simulations

Figure 28 shows a PS-PMT resistor chain with N anode wires interconnected by resistors. R_i is the resistance of the i^{th} inter-anode resistor in the chain. To develop the impulse response h(n), of the resistor chain, we assume that all the charge is deposited on a single anode wire A_n, where $1 \le n \le N$. The position output is given by the impulse response h(n) of the readout. Since both ends of the resistor chain are tied to virtual ground, the charge at A_n is divided according to the voltage divider formed by the resistor chain at A_n. Equation(31) gives the charge division impulse response for arbitrary resistor chain values.

$$h(n)=\frac{\sum_{i=n}^{N} R_i-\sum_{i=0}^{n-1} R_i}{\sum_{i=0}^{N} R_i}$$

(31)

The charge distribution can be modeled as a unit area Gaussian distribution described in equation(30). Convolving the impulse response h(n), with the section of the charge distribution function $\Gamma(n,\mu)$, which projects onto the anode wires, results in equation(32) describing the actual readout.

$$\begin{aligned} X'(\mu) &= h(n)*\Gamma(n,\mu) \\ &= \sum_{n=1}^{N} h(n)\Gamma(n,\mu) \end{aligned}$$

(32)

Using equation(32) as a model of the PS-PMT resistor chain readout, we simulated the effect of modifying the x-axis resistor chain of a Hamamatsu R-3941 PS-PMT. The x-axis of this tube has 18 anode wires (N=18), with a standard anode wire resistor chain composed of 1k**Ω** resistors ($R_0 \ldots R_{18}$=1k**Ω**). Using the above values and assuming a charge spread similar to that found in Figure 26 (σ=1.67), we simulated the effect of increasing the resistance of R_1 & R_{17}.

In Figure 29 we see the double valued readout near the periphery of the PS-PMT with the unmodified readout. As the value of R_1 & R_{17} was increased from 1k**Ω** to 4.7k**Ω** and then 15k**Ω**, the effect of the lost charge is compensated, and resulted in an overall increase in the field-of-view. However, the position accuracy was reduced in the central portion of the field-of-view.

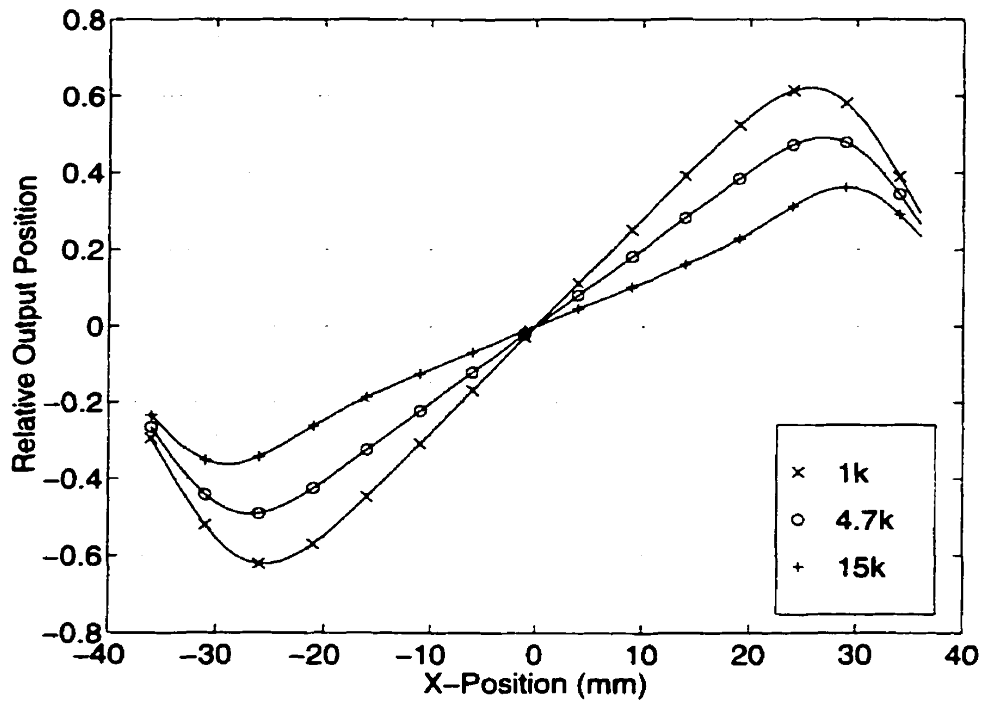

Figure 29 Simulation of resistor chain modification showing the effect of increased resistance between adjacent peripheral anode wires on readout linearity and field-of-view.

4.3 Experimental Methods

Modifications were made to the resistor chain on the printed circuit board of a Hamamatsu R-3941 crossed anode wire PS-PMT [36]. Two resistors from each end of the x-axis resistor chain (R_1 & R_{17}) and two from the y-axis resistor chain (R_1 & R_{15}) were removed and sockets were put in their place allowing different resistor values to be placed in the resistor chains. Data was acquired using the standard current amplifier circuit of **Error! Reference source not found.**, and event positioning was established via equation (29). The crystals were irradiated using a 511 keV γ-ray source. Data was collected using a Jorway Aurora14 ADC [62] acquisition system.

4.3.1 Readout Linearity

A holder was machined in order to mount eleven 3×10×30 mm polished BGO crystals onto the PS-PMT face spanning the x-axis in a straight line at the mid y-axis level. The crystals were oriented such that the 3×10 mm^2 area was optically coupled to the PS-PMT face with only the 3 mm side profile projecting onto the x-axis. The center-to-center crystal separation was 6.75 mm and all crystals were wrapped in a reflective coating of Teflon tape in order to optically isolate the crystals and to maximize light transmission to the photocathode [75,76]. X-axis crystal position readout was recorded and compared with the actual crystal position. For crystals near the periphery of the tube face where the output positioning was double valued, the experiment was repeated with only one edge crystal in place, thereby allowing the positioning of these edge elements to be recorded.

4.3.2 Pixellated Crystal Identification

A second experiment was performed using the cut BGO crystal blocks developed for use in the Montreal Neurological Institute's PEM scanner [7,42,77]. These 36×36×20 mm BGO crystals have two matrices of 2×2 mm elements cut into the top and bottom of the crystal, offset from one another by 1 mm in each direction (see Figure 12). The top elements (furthest from the photocathode) are 11.5 mm deep while the bottom elements (closest to the photocathode) are 7.5 mm deep, leaving a 2 mm thick layer connecting the two matrices. A potting compound optically isolates adjacent crystal elements and maximizes light transmission to the photocathode [42].

Four such BGO blocks were optically coupled to a Hamamatsu R-3941 PS-PMT and side irradiated using a highly collimated 511 keV γ-ray source [41,42] which was oriented such that only the crystals closest to the photocathode were irradiated. A semi-automated crystal identification routine [42] was used to identify the BGO block crystal elements.

4.4 Results

4.4.1 Readout Linearity

Figure 30 shows the relative positioning output versus the actual crystal position for the x-axis. Results were obtained for 3 different resistor chain configurations:

- $R_0 \ldots R_{18} = 1k\Omega$ (standard readout)
- $R_0, R_2 \ldots R_{16}, R_{18} = 1k\Omega$ R_1 & $R_{17} = 4.7k\Omega$
- $R_0, R_2 \ldots R_{16}, R_{18} = 1k\Omega$ R_1 & $R_{17} = 15k\Omega$

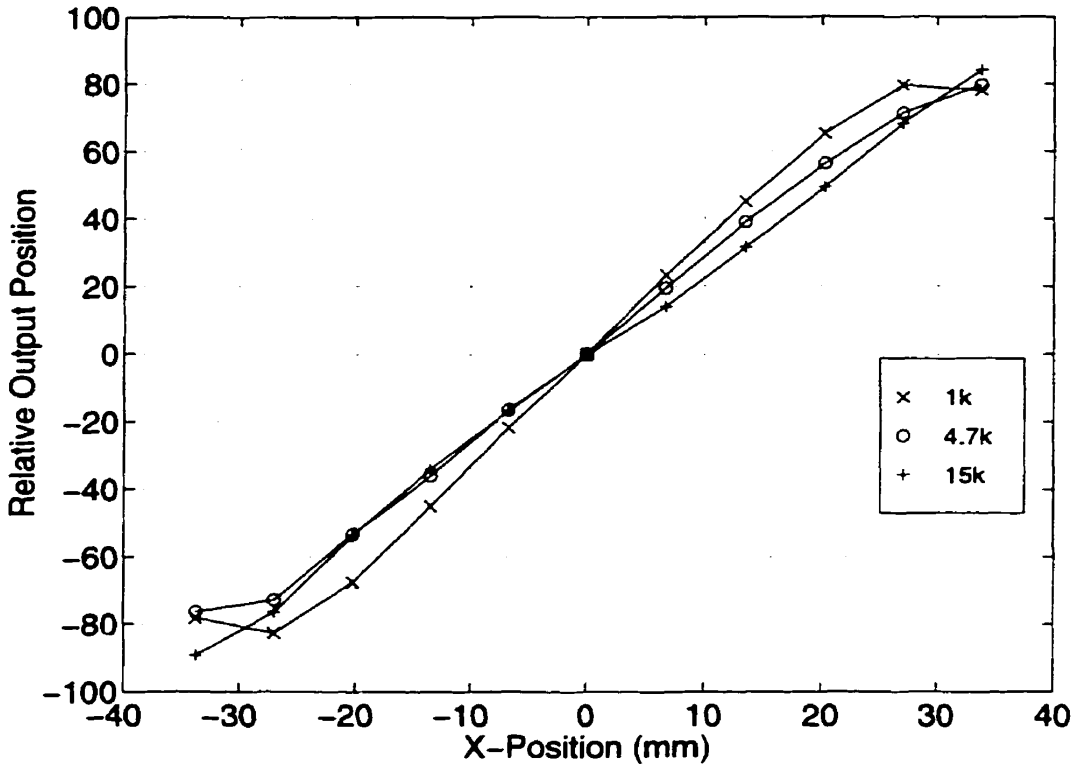

Figure 30 Resistor chain readout obtained using different resistor values used between the end anode wires.

Using the all-1kΩ unmodified resistor chain readout, the central portion of the PS-PMT face had high position accuracy. However, near the edges of the field-of-view the positioning readout was no longer single valued. The "folding over" of the readout near the periphery makes crystal identification and event positioning impossible in those regions, thereby reducing the effective field-of-view. Increasing the resistance of R_1 & R_{17} to 4.7kΩ and leaving the rest of the chain unchanged improved the readout. It became single valued throughout, but had low accuracy at the extrema. In addition, the accuracy in the central portion was less than that from the unmodified readout. Setting R_1 & R_{17} to 15kΩ dramatically improved the readout. Not only was the readout single valued

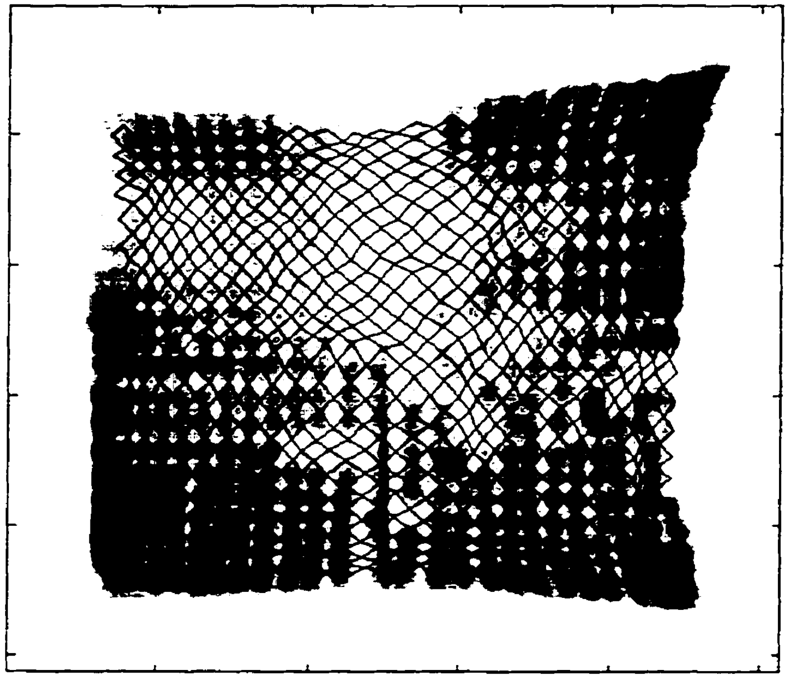

Figure 31 Crystal element identification routine result, using an unmodified, all 1kΩ resistor chain. 24 rows were identified in the x-axis and 20 columns were identified in the y-axis.

throughout, but also the range of linear readout extended across the field-of-view. Further increasing R_1 & R_{17} lowered the position accuracy in the center of the field-of-view, overcompensated for charge loss at the edges of the periphery of the x-axis and made the readout in that region non-linear.

4.4.2 *Pixellated Crystal Identification*

With the original unmodified readout arrangement, 24 rows in the x-axis and 20 columns of crystals in the y-axis were identified (see Figure 31) on the near face of the PS-PMT. The fishnet-checkerboard array represents boundary assignments for both near and far crystals. Event pile-up resulting from the double valued nature of the unmodified readout can be observed in the lower left and upper right corners of the image.

After increasing the end resistors R_1 & R_{17} in the x-axis and R_1 & R_{15} in the y-axis, from 1kΩ to 15kΩ additional crystal rows and columns from the near face of the crystal block were identified bringing the count to 29 rows in the x-axis and 23 columns in the y-axis (see Figure 32). This corresponds to an overall increase in the field-of-view of 39%.

4.5 Discussion

The results of the linear readout experiment (see Figure 30) closely match those predicted by equation(32) which are shown in Figure 29. The experimental

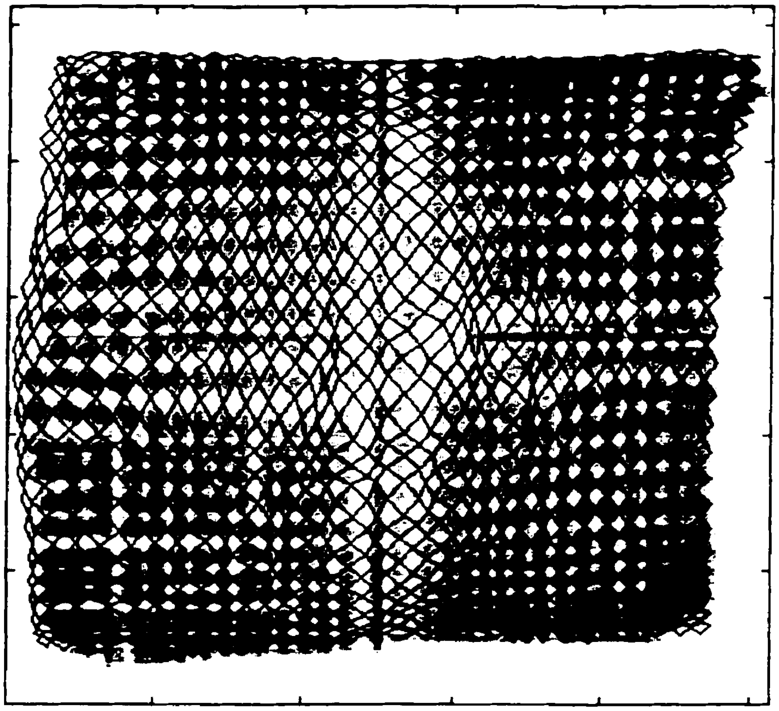

Figure 32 Crystal element identification routine results using a modified resistor chain. Peripheral inter-anode wire resistors were set to 15kΩ and all others 1kΩ. 29 rows were identified in the x-axis and 23 columns were identified in the y-axis.

results validate the original assumptions of a small symmetric light spread distribution directly below the crystals onto the anode wires, and of the truncation and subsequent loss of the charge extending past the last anode edge wires. Figure 30 shows that as the value of the resistance between the end anode wires (R_1 & R_{17} for the x-axis) is increased, the charge reaching the peripheral anode wires is redistributed, partially compensating for the lost charge. Increasing the resistance at the periphery also has the effect of decreasing the position accuracy at the center of the field-of-view of the PS-PMT. However, since the position readout accuracy in that region is already quite high, modification of the resistor chain has a negligible effect on crystal identification in the central region.

Additional experiments were carried out exploring the potential benefit of changing additional resistors from the resistor chain. R_2 & R_{16} from the x-axis were modified to better fit the Gaussian charge distribution charge loss. Experiments using resistance values of 3kΩ and 5kΩ were performed. However, minimal improvements were observed.

Figure 32 shows the improved field-of-view over the standard unmodified readout Figure 31. A gain in the field-of-view of 10 mm in the x-axis and 6 mm in the y-axis was obtained simply by modifying the resistance of the last resistors in each chain to 15kΩ, increasing the overall field-of-view by 39%. This increase is especially important in applications such as the positron emission mammography system our group is currently developing [77]. It not only allows a greater area of the breast to be imaged at one time, and it gives the PS-PMT the potential to image breast tissue significantly closer to the chest wall.

CONCLUSION

The MNI-PEM scanner is a high-resolution functional imaging system designed to be used in conjunction with a conventional mammography unit in order to detect cancerous tumors and reduce the number of unnecessary needle biopsies. The scanner uses two Hamamatsu R-3941 crossed anode wire PS-PMT detectors. These detectors are placed across from one another on either side of the breast of interest. Since the detectors are placed next to the chest, the dead space surrounding the field-of-view limits the ability of the scanner to detect tumors located near the chest wall. Exploration into methods of improving the field-of-view and reducing the dead-space of the MNI-PEM detectors forms the basis of this thesis.

Multi-anode PS-PMT based block detectors such as those used in the MNI-PEM scanner have a much greater spatial resolution than is found in traditional single-anode PMT based block detectors. However, this increase in performance comes at the cost of a larger number of anode signals to be processed. We examined two readout methods for crossed-anode wire PS-PMTs that could maximize the potential of the MNI-PEM scanner: a modified Anger logic resistor chain readout and a targeted sparse multi-channel readout.

The first method is a modified Anger logic resistor chain readout. Like all centroid-based readouts of PS-PMTs, this method offers an excellent compromise between maintaining high spatial resolution and minimizing readout complexity. For many applications, standard Anger logic readouts are the method of choice. However, as a result of the truncation of the charge which extends past the edge anode wire, the linearity of the readout quickly degrades for events located near the periphery of the PS-PMT, even becoming double-valued on occasion. This significantly reduces the usable area of the photocathode. Of particular concern for the MNI-PEM scanner is the fact that this truncation of charge limits its ability to effectively detect tumors located near the chest wall.

In order to compensate for this lost charge, we have shown that a very simple modification to the Anger logic anode wire resistor chain can significantly improve the field-of-view of a crossed anode wire PS-PMT. Increasing the resistance in the anode resistor chain between the extreme anode wires can partially compensate for the loss of charge beyond the anode wires of PS-PMTs. Simply changing four resistors from 1 kΩ to 15 kΩ increased the field-of-view by 39%.

A multi-channel readout method was also explored. Previous research has shown that by collecting signals from all of the individual anode wires and using a Gaussian peak-fitting algorithm, a linear readout across the entire photocathode area of the PS-PMT can be achieved. This approach seems to have the potential to maximize the ability of the MNI-PEM detector to identify tumors near the chest wall. Unfortunately, multi-channel readouts are very complex when implemented in parallel, and have large dead times when implemented as serial readouts. We therefore chose to explore the potential of a hybrid multi-channel readout: the sparse targeted readout.

The sparse targeted readout dynamically digitizes only the 6 anode signals that surround the event center for each channel. The channel selection is determined by a WTA integrated circuit. It examines the analog voltages of the sampled peak of the integrated anode signals and produces the digital address of the peak location. This method has the potential to significantly increase the usable field-of-view of the MNI-PEM detector while still functioning at high data rates. Unfortunately, due to fabrication problems with the WTA circuit, this method was never tested on an actual PEM detector.

Given the difficulties encountered while fabricating the WTA IC, and the relative simplicity and effectiveness of the modified Anger logic resistor chain readout method, this technique was chosen for use in the MNI-PEM scanner. Both detector modules were modified in order to compensate for the lost charge extending past the end anode wires. The modified PEM scanners are able to gather an image area of the breast that is 39% larger. More importantly, the system is now able to collect counts from events 5 mm closer to the chest wall than was previously possible. This reduction in detector dead space enables the MNI-PEM scanner to be more effective in its role of identifying cancerous cells. The modified resistor chain has been in use for more than two years with readouts remaining stable and consistent over this period.

In conclusion, it should be noted that this investigation into improved readout methods has yielded several interesting results. First, minimal modifications to the Anger logic resistor chain yielded significant improvements in the field-of-view compared to the standard readout method. These modifications can easily be implemented and they have proven robust and reliable with over two years of clinical use. Secondly, although a sparse targeted readout scheme was never tested, the concept merits future research. The availability of new low cost analog to digital converters along with flexible field programmable gate arrays make a digital implementation of the sparse targeted readout very attractive.

REFERENCES

[1] Data taken from National Cancer Institute of Canada: Canadian Cancer Statistics 1997.

[2] C.J. Thompson, K. Murthy, I.N. Weinberg, F. Mako "Feasibility Study for Positron Emission Mammography" *Med. Phys. vol 21, num. 4*, 1994, pp. 529-538.

[3] C.S. Levin, E.J. Hoffman, M.P. Tornai, L.R. MacDonald "PS-PMT and Photodiode Design of a Small Scintillation Camera for Imaging Malignant Breast Tumors" *IEEE Trans. Nucl. Sci., vol. 44, no. 4,* 1997.

[4] W.W. Moses, T.F. Budinger, R.H. Huesman, S.E. Derenzo "PET Camera Designs for Imaging Breast Cancer and Axiliary Node Involvement" *J. Nucl. Med., vol. 36, num. 5,* 1995, p. 69.

[5] R.L Wahl, R.L. Cody, G.D. Hutchins, E.E. Mudgett "Primary and Metastic Breast Carcinoma: Initial Clinical Evaluation with PET with the Radiolabeled glucose analogue 2-[^{18}F]-fluoro-2-deoxy-D-glucose" *Radiology, vol. 179,* 1991, pp. 756-770.

[6] A.H. McGuire, F. Dehdasti, B.A. Siegel, A.P. Lyss, J.W. Brodack, C.J. Mathias, M.A. Mintun, J.A. Katzenellenbogen, M.J. Welch, "Positron Tomographic Assessment of 16a-[^{18}F]-fluoro-17b-estradiol Uptake in Metastic Breast Carcinoma" *J. Nucl. Med., vol. 32, num. 8,* 1991, pp. 1562-1531.

[7] C.J. Thompson, K. Murthy, Y. Picard, I.N. Weinberg, R. Mako "Positron Emission Mammography (PEM) A Promising Technique for Detecting Breast Cancer" *IEEE Trans. Nucl. Sci. vol. 42, no. 4,* 1995, pp. 1012-1017.

[8] T.F. Budinger, S.E. Derenzo, G.T. Gullberg, W.L. Greenberg, R.H. Huesman "Emission Computer Assisted Tomography with Single-Photon and Positron Annihilation Photon Emitter" *Journal of Computer Assisted Tomagraphy, vol. 1,* 1977, pp. 131-145.

[9] S.E. Derenzo "Recent Developments in Positron Emission Tomography (PET) Instrumentation" *SPIE* vol. 671, 1986, pp. 232-243.

[10] W.R. Cook, M.Finger, T.A. Prince "A Thick Anger Camera for Gamma-ray Astronomy" *IEEE Trans. Nucl. Sci. vol. 32, no. 1,* 1985, pp. 129-133.

[11] "Photomultiplier Handbook" *Burle Industries, Inc., Tube Produst Division*, 1000 New Holland Ave., Lancaster, PA, USA, 1980.

[12] Hamamatsu Photonics "Photomuliplier Tubes" Hamamatsu Photonics K.K., 325-6, Sunayama-cho, Hamamatsu city, 430, Japan, 1994.

[13] R.H. Redus, V. Nagarkar, L.J. Cirignano, W. McGann, M.R. Squillante "A Nuclear Survey Instrument with Imaging Capability" *IEEE Trans. Nucl. Sci., vol. 39, no. 4,* 1992, pp. 948-951.

[14] H.E. Johns, J.R. Cunningham, The Physics of Radiology, 4th ed., Charles C. Thomas, New York, 1983.

[15] Philips Photonics, "Photomultiplier Tubes: Principles and Applications" Produced and distributed by Philips Photonics, International Marketing, BP 520, F-19106 Brive, France, 1994

[16] "Electro-Optics Handbook" *Burle Industries, Inc., Tube Produst Division*, 1000 New Holland Ave., Lancaster, PA, USA, 1992.

[17] C.L Melcher, J.S. Schweitzer "Cerium-doped Lutetium Oxyorthosilicate: A Fast, Efficient New Scintillator" *IEEE Trans. Nucl. Sci., vol. 39,* 1992, pp. 502-505.

[18] R. Daghighian, D.M. Lovelock, B. Eshaghian, P. Shevderov, J.D. Willins "Design Considerations of an Animal PET Scanner Utilizing LSO Scintillators and Position Sensitive PMTs" *IEEE Nucl. Sci & Med. Imag. Conf. Rec.* vol 3, 1994.

[19] J.E. Litton, S. Holte, L. Eriksson "Evaluation of the Karolinska New Positron Camera System; The Scanditronix PC2048-15B" *IEEE Trans. Nucl. Sci.,* vol. 37, no.2, April, 1990, pp. 743-748.

[20] W.M. Digby, M. Dahlbom, E.J. Hoffman "Detector, Shielding and Geometric Design Factors for a High-Resolution PET System" *IEEE Trans. Nucl. Sci.* vol. 37, no.2, April, 1990, pp. 664-670.

[21] T.F. Budinger, K.M. Brennan, W.W. Moses S.E. Derenzo "Advances in Positron Tomography for Oncology" *Nucl. Med. & Bio.* vol. 23, 1996, pp. 659-667.

[22] V.K. Zworykin, G.A. Morton, L. Malter "The Secondary Emission Multiplier: A New Electronic Device" *Proc. IRE, vol. 23, pp. 55-64,* 1935.

[23] S.E. Derenzo "Initial Characterization of a BGO-Photodiode Detector for High Resolution Positron Emission Tomography" *IEEE Trans. Nucl. Sci.,* vol. 31, no.1, February, 1984, pp. 620-626.

[24] R. Lecomte, D. Schmitt, A.W. Lightstone, R.J. McIntyre "Performance Characteristics of BGO-Silicon Avalanche Photodiode Detectors for PET" *IEEE Trans. Nucl. Sci.* vol. 32, no.1, 1985, pp. 482-486.

[25] C. Carrier, C. Martel, D. Schmitt, R. Lecomte "Design of a High Resolution Positron Emission Tomograph Using Solid State Scintillation Detectors" *IEEE Trans. Nucl. Sci.* vol. 35, no. 1, 1988, pp. 685-690.

[26] R. F. Pierret, Semiconductor Fundamentals: Modular Series on Solid State Devices, 2nd ed., Addison-Wesley Publishing Company, New York., 1989.

[27] Philips Photonics "XP1700: Multi-Channel Photomultipliers" Product description. Produced and distributed by Philips Photonics, International Marketing, BP 520, F-19106 Brive, France.

[28] H. Uchida, T. Yamashita, M. Iida, S. Muramatsu "Design of a Mosaic BGO Detector System for Positron CT" *IEEE Trans. Nucl. Sci.* vol. 33, no. 1, February, 1986, pp. 464-467.

[29] S. Suzuki, T. Matsushita, T. Suzuki, S. Kimura, H. Kume "New Position Sensitive Photomultiplier Tubes for High Energy Physics and Nuclear Medical Applications" *IEEE Trans. Nucl. Sci. vol. 35, no. 1*, 1988, pp. 382-386.

[30] Y.Shao, S.R. Cherry, S. Siegel, R.W. Silverman "Evaluation of Multi-Channel PMT's for Readout of Scintillator Arrays" *Nucl. Inst. Meth. A vol. 390,* 1997, pp. 209-218.

[31] Philips Photonics "XP1700:Multi-Channel Photomultipliers" Product description. Produced and distributed by Philips Photonics, International Marketing, BP 520, F-19106 Brive, France.

[32] M. Singh, R. Leahy, K. Oshio, R.R. Brechner, X. Hong Yan "A New Generation of SPECT and PET Systems Based on Position Sensitive Photomultipliers" *IEEE Trans. Nucl. Sci.* vol. 37, no. 3, 1990, pp. 1321-1327.

[33] R. Daghighian, D.M. Lovelock, B. Eshaghian, P. Shevderov, J.D. Willins "Design Considerations of an Animal PET Scanner Utilizing LSO Scintillators and Position Sensitive PMTs" *IEEE Nucl. Sci & Med. Imag. Conf. Rec.* vol 3, 1994.

[34] S.R. Cherry, Y. Shao, S. Siegel, R.W. Silverman, E. Mumcuoglu, K. Meadors, M.E. Phelps "Optical Fiber Readout of Scintillator Arrays Using a Multi-Channel PMT: A High Resolution PET Detector for Animal Imaging" *IEEE Trans. Nucl. Sci.,* vol. 43, no. 3, 1996, pp. 1932-1937.

[35] S. Siegel, R.W. Silverman, S.R. Cherry "Simple Charge Division Readouts for Imaging Scintillator Arrays Using a Multi-Channel PMT" *IEEE Trans. Nucl. Sci., vol.43*, 1996, pp. 1634-1641.

[36] R-3941 PS-PMT is manufactured by Hamamatsu Photonics K.K., 325-6, Sunayama-cho, Hamamatsu city, 430, Japan.

[37] R.L. Clancy, C.J. Thompson, J.L. Robar, A.M. Bergman "A Simple Technique to Increase the Linearity and Field-of-View in Position Sensitive Photmultiplier Tubes" *IEEE Trans. Nucl. Sci.*, vol. 44, no. 3, 1997, pp. 494-498.

[38] A. Truman, A.J. Bird, D. Ramsden, Z. He "Pixellated CsI(Tl) Arrays with Position-Sensitive PMT Readout" *Nuclear Instruments and Methods in Physics Research A*, no. 353, 1994, pp 375-378.

[39] M.B. Williams, R.M. Sealock, S. Majewski, A.G. Weisenberger "High Resolution PET Detector Using Wavelength Shifting Optical Fibers and Microchannel Plate PMT with Delay Line Readout" *IEEE Trans. Med. Imag.*, 1997 (submitted)

[40] A.J. Bird, Z. He, D. Ramsden "Multi-Channel Readout of Crossed-Wire Anode Photmulipliers" *Nuclear Instruments and Methods in Physics Research A*, no. 348, 1994, pp. 668-672.

[41] J.L. Robar, C.J. Thompson, K. Murthy, R.L. Clancy, A.M. Bergman "Construction and Calibration of Detectors for High-Resolution Metabolic Breast Imaging" *Nuclear Instrumentation and Methods in Research A 392, 1997, pp. 402-406.*

[42] J.L. Robar "Construction and Calibration of Detectors for High-Resolution Metabolic Breast Cancer Imaging" *M.Sc. Thesis, Med. Physics Unit, McGill University*, 1996.

[43] S. Pavlopoulos, G. Tzanakos "Desing and Performance Evaluation of a High-Resolution Small Animal Positron Tomograph" *IEEE Trans. Nucl. Sci., vol. 43, no. 6*, 1996, pp. 3249-3255.

[44] M.E. Casey, R. Nutt, "A Multicrystal Two Dimensional BGO Detector System for Positron Emission Tomography" *IEEE Trans. Nucl. Sci., vol. 33, pp. 460-463*, 1986,

[45] W.M. Digby, M. Dahlbom, E.J. Hoffman "Detector, Shielding and Geometric Design Factors for a High-Resolution PET System" *IEEE Trans. Nucl. Sci., vol. 37, no. 2*, 1990, pp. 664-670.

[46] M. Dahlbom, E.J. Hoffman "An Evaluation of a Two-Dimensional Array Detector for High Resolution PET" *IEEE Trans. Med. Imag., vol. 7, no. 4,* 1988, pp. 264-271.

[47] M.P. Tornai, G. Germano, E.J. Hoffman "Positionaing and Energy Response of PET Block Detectors with Different Light Sharing Schemes" *IEEE Trans. Nucl. Sci., vol. 41, no. 4,* 1994, pp. 1458-1463.

[48] A. Del Guerra, F. de Notaristefani, G. Di Domenico, M. Giganti, R. Pani, A. Piffanelli, A. Turra, G. Zavattini "Use of a YAP:Ce Matrix Coupled to a Position-Sensitive Photomultiplier for High Resolution Positron Emission Tomography" *IEEE Trans. Nucl. Sci., vol. 43, no. 3,* 1996, pp. 1958-1962.

[49] S.R. Cherry, Y. Shao, R.W. Silverman, A. Chatziioannou, K. Meadors, S. Siegel, T. Farquhar, J. Young, W.F. Jones, D. Newport, C. Moyers, M. Andreaco, M. Paulus, D. Binkley, R. Nutt, M.E. Phelps "MicroPET: A High Resolution PET Scanner for Imaging Small Animals" *IEEE Trans. Nucl. Sci., vol. 44,* 1997, pp.1161-1166.

[50] L.P. Adler, J.P. Crowe, N.K. Al-Kaisi, J.L. Sunshine "Evaluation of Breast Masses and Axillary Lymph Nodes with F-18-2-deoxy-fluoro-D-glucose PET" *Radiology, vol. 187,* 1993, pp. 743-750.

[51] A.M. Bergman "Evaluation of a Positron Emission Mammography (PEM) System Using Images Co-Registered with X-Ray Mammograms" *M.Sc. Thesis, Med. Physics Unit, McGill University,* 1997.

[52] J.E. Litton, s. Holte, L. Eriksson "Evaluation of the Karolinska New Positron Camera System; The Scanditronix PC2048-15B" *IEEE Trans. Nucl. Sci., vol. 37, no. 2,* 1990, pp. 743-748.

[53] S.V. Guru, Z. He, D.K. Wehe, G.F. Knoll "A Portable Gamma Camera for Radiation Monitoring" *IEEE Trans. Nucl. Sci., vol. 42, no. 1,* 1995 pp. 367-370.

[54] H.O. Anger "Scintillation Camera" *Rev. Sci. Inst.,* vol 29, no. 1, 1958, pp. 27-33.

[55] Hamamatsu Technical Data: "Position-Sensitive Photomultiplier Tubes with Crossed Wire Anodes R2487 series" Hamamatsu Photonics K.K., 325-6, Sunayama-cho, Hamamatsu city, 430, Japan.

[56] P. Olivier, Personal communications: Park Medical Systems Inc., November, 1996.

[57] Y. Nagai, H. Saito, T. Hyodo, H. Uchida, T. Omura "Positron Sensitive Scintillation Detectors for γ-Rays" *Materials Science Forum*, vols. 175-178, 1995, pp. 971-974.

[58] R.L. Clancy, C.J. Thompson, J.L. Robar, K. Murthy, E. Beuville, W.W. Moses "Targeted Sparse Readout for Multi-Anode Photomultipliers and Optically Isolated Crystals" *IEEE Nucl. Sci. Symp. Conf. Rec., 1995,* pp. 409-411.

[59] R-2487 PS-PMT is manufactured by Hamamatsu Photonics K.K., 325-6, Sunayama-cho, Hamamatsu city, 430, Japan.

[60] R-3292 PS-PMT is manufactured by Hamamatsu Photonics K.K., 325-6, Sunayama-cho, Hamamatsu city, 430, Japan.

[61] IEEE/ANSI STD 583-1982: "IEEE Standard Modular Instrumentation and Digital Interface System (CAMAC)" IEEE, 1981.

[62] Aurora 14 ADC is manufactured by Jorway Corporation, 27 Bond St., Westbury, NJ 11590.

[63] B. Sekerkiran, U. Cilingiroglu "High Resolution CMOS Winner-Take-All Circuit" *IEEE International Conference on Neural Networks – Conference Proceedings,* vol. 4, 1995, pp. 2023-2026.

[64] J. Choi, B.J. Sheu "A High-Precision VLSI Winner-Take-All Circuit for Self-Organizing Neural Networks" *IEEE Journal of Solid-State Circuits*, vol. 28, no. 5., 1993, pp. 576-583.

[65] W.W. Moses, E. Beuville, M.H. Ho "A 'Winner-Take-All' IC for Determining the Crystal of Interaction in PET Detectors" *IEEE Trans. Nucl. Sci., vol. 43, no. 3*, 1996, pp. 1615-1618.

[66] W.W. Moses, I. Kipnis, M.H. Ho, "A 16-Channel Charge Sensitive Amplifier IC for a PIN photdiode Array Based PET detector Module" *IEEE Transactions on Nuclear Science*, vol. 41, no. 4, August 1994, pp. 1469-1472.

[67] S. Smedley, J. Taylor, M. Wilby "A Scalable High-Speed Current-Mode Winner-Take-All Network for VLSI Neural Applications" *IEEE Transactions on Circuits & Systems-1: Fundamental Theory and Applications*, vol. 42, no. 5, May 1995, pp. 289-291.

[68] Canadian Microelectronics Corporation: 210A Carruthors Hall, Queen's University, Kingston, Canada, K7L 3N6

[69] A.B. Grebeen, Bipolar and MOS Analog Circuit Design, John Wiley & Sons, Inc., 1984.

[70] Analog Devices Inc. "Analog Devices Data Converter Reference Manual Volume II" Analog Devices, One Technology Way., P.O. Box 9106, Norwood, MA, 02062, USA.

[71] N.J. Yasillo, R.N. Beck, M. Cooper "Design Considerations for a Single Tube Gamma Camera" *IEEE Trans. Nucl. Sci. vol. 37, no. 2,* 1990, pp. 609-612.

[72] M. Watanabe, T. Omura, H. Kyushima, Y. Hasegawa, T. Yamashita "A Compact Position-Sensitive Detector for PET" *IEEE Trans. Nucl. Sci.,* 1995, pp. 1090-1094.

[73] S. Weber, A. Terstegge, H. Halling, H. Herzog, R. Reinartz, P. Reinartz, F. Rongen, H.W. Muller-Gartner "The Design of an Animal PET: Flexible Geometry for Achieving Optimal Spatial Resolution or High Sensitivity" *IEEE Med. Imag. Conf. Rec., 1995,* pp. 1002-1005.

[74] H. Kume, S. Muramatsu, M. Iida "Position Sensitive Photomultiplier Tubes for Scintillation Imaging" *IEEE Trans. Nucl. Sci., vol. 33, no. 1,* 1986, pp. 359-362.

[75] S.R. Cherry, Y. Shao, M.P. Tornai, S. Siegel, A.R. Ricci, M.E. Phelps, "Collection of Scintillation Light from Small BGO Scintillators" *IEEE Trans. Nucl. Sci., vol. 42,* 1995, pp. 1058-1063.

[76] C. Carrier "Mémoire de Maîtrise: Etude de la Collecte de Lumière dans les Cristaux à Scintillation Utilisés en Tomographie d'Emission" M.Sc. thesis, University of Sherbrooke, 1988.

[77] C.J. Thompson, K. Murthy, R.L. Clancy, J.L. Robar, A.M. Bergman, R. Lisbona, A. Loutfi, J.H. Gagnon, I.N. Weinberg, R. Mako "Imaging Performance of PEM-1: A High Resolution System for Positron Emission Mammography" *IEEE Med. Imag. Conf. Rec.,* 1995, pp. 1074-1078.